ADVANCING METHODS FOR IN VIVO NEUROCHEMICAL MONITORING

by

Elaine Marie Robbins

B.S. Biochemistry, American University, 2012

Submitted to the Graduate Faculty of the

Kenneth P. Dietrich School of Arts and Sciences in partial fulfillment

of the requirements for the degree of

Doctor of Philosophy

University of Pittsburgh

2019

UNIVERSITY OF PITTSBURGH

KENNETH P. DIETRICH SCHOOL OF ARTS AND SCIENCES

This dissertation was presented

by

Elaine Marie Robbins

It was defended on

July 26, 2019

and approved by

Shigeru Amemiya, Professor, Department of Chemistry

Alexander Star, Professor, Department of Chemistry

Xinyan Tracy Cui, Professor, Department of Bioengineering

Dissertation Advisor: Adrian Michael, Professor, Department of Chemistry

ADVANCING METHODS FOR IN VIVO NEUROCHEMICAL MONITORING

Elaine Marie Robbins, PhD

University of Pittsburgh, 2019

Dopamine is a neurotransmitter involved in both normal and pathological brain function. Modeling dopamine responses measured with fast scan cyclic voltammetry can provide insight into dopamine's function. Dopamine responses are broadly categorized as fast and slow, based on the amount of time between when the stimulus starts and when dopamine is detected. By changing the amount of time between a stimulus pulse and a dopamine-detecting waveform, we determined that slow-responding sites are due to differences in kinetics between fast and slow sites, not a gap between the recording electrode and dopamine terminals. Additionally, with the use of the D2 antagonist raclopride and advances in the restricted diffusion model for dopamine dynamics, we show that slow sites are caused by an underlying autoinhibitory tone that fast sites do not have.

In addition, this work explores metabolic changes after traumatic brain injury. Traumatic brain injury is divided into a primary insult and a secondary injury, like spreading depolarization, that causes further damage over time. Spreading depolarizations – waves of uncontrolled depolarization followed by energy-consuming repolarization – can cause the injury lesion core to spread into the comparatively healthy surrounding tissue. Monitoring glucose and potassium as markers of spreading depolarization waves can be accomplished by microdialysis; however, immune response to the injury caused by implantation greatly diminishes the temporal sampling window. Previous work has established that five days of retrodialysis with dexamethasone

mitigates this immune response and greatly increases the probe lifetime. Traumatic brain injury model rats and rapid sampling microdialysis were employed to monitor glucose and potassium levels continuously for ten days after injury. Short term metabolic crises, like spreading depolarization, were observed in injured animals. Additionally, in almost every case, glucose concentrations declined slowly over several days to undetectable levels and did not recover during the timespan of the experiment, despite histology confirming that there is living tissue around the probe ten days after implantation.

TABLE OF CONTENTS

LIST OF TABLES

LIST OF FIGURES

LIST OF EQUATIONS

1.0   INTRODUCTION

1.1   IMPLANTED NEUROMONITORING DEVICES

Brain-implanted measurement devices are invaluable tools for neuromonitoring. Devices such as intercranial pressure monitors are standards of care for patients with brain injuries like stroke and traumatic brain injury (TBI).[1–3] In research contexts, implanted electrodes and sampling probes provide valuable insight into brain function in animal models and in clinical settings.[4–7] Cutting edge implanted neuroprosthetics now allow quadriplegic patients to move robotic arms and even feel a sense of touch through feedback from the artificial limb.[8–10] However, insertion of a foreign body into brain tissue inherently causes a response by the tissue. Some devices, like carbon fiber microelectrodes, are constructed to be small enough that their implantation causes no immune response.[11,12] Others, like microdialysis probes, are much larger and cause a cascade of effects culminating in a nonfunctional device.[11,13–15] Both carbon fiber microelectrodes and microdialysis probes will be discussed in detail in this work. Measurements of dopamine (DA) made with carbon fiber microelectrodes reveal kinetic details that can be interpreted with mathematical modeling.[16–18] Microdialysis, and the challenges involved in mitigating the immune responses to the probe implantation, will also be discussed; particularly, measurements of glucose and potassium in the context of TBI.

1.2   DOPAMINE

DA is an incredibly important catecholamine neurotransmitter that is involved in many functions in both healthy and diseased brains, including movement, reward, and addiction.[19,20] First synthesized by Mannich and Jacobsohn in 1910,[19,21] DA's importance was recognized in 1958 when Carlsson and coworkers proved that DA is a neurotransmitter.[22,23] DAergic neurons follow multiple circuits in the brain, but in this work a single circuit will be focused on, namely the midbrain DAergic neurons of the nigrostriatal pathway. The cell bodies of nigrostriatal neurons are located in the substantia nigra. From here, their axons run through the medial forebrain bundle (MFB) and terminate in the dorsal striatum (DS).[19] Electrical stimulation of the MFB, performed in the experiments described in Chapters 2 and 3, results in a release of DA into the DS. Additionally, in Chapter 4 DAergic projections from the ventral tegmental area (VTA) to the ventral striatum (VS) will be examined. Dysfunction of these pathways is involved in many disorders, including Parkinson's disease, addiction, and attention deficit hyperactivity disorder.[19,24–29] DA is synthesized from the nonessential amino acid L-tyrosine, which is converted to L-3,4-dihydroxyphenylalanine (L-DOPA) by tyrosine hydroxylase (TH), and finally to DA by DOPA decarboxylase. It is degraded to homovanillic acid (HVA) by monoamine oxidase and catechol-O-methyltransferase (COMT) with either 3,4-dihydroxyphenylacetic acid (DOPAC) or 3-methoxytyramine (3-MT) as intermediates depending on the order of degradation.[19]

DA is released into the synapse from the vesicles in which it is stored.[30] A basic schematic of this process is shown in Figure 1-1. Vesicles are divided into three pools: the readily releasable pool, the recycling pool, and the reserve pool.[30,31] These pools are classified

based on how quickly they can release their contents. The readily releasable pool can be released immediately upon stimulation. These vesicles are already docked onto the membrane and the soluble N-ethylmaleimide sensitive fusion protein attachment protein receptor (SNARE) proteins are already configured for release. Further stimulation will result in the release of the recycling pool, and only prolonged stimulation will cause the release of the reserve pool. In the DS, synapses occur approximately once every 3.5 µm on average.[32] Synaptic junctions have been estimated to be approximately 300 nm long and 15 nm wide.[33]

Various receptors and transporters control DA signaling, and receptors on both the pre- and post-synaptic neurons are triggered.[34] Receptors are divided into two families: the D1 family of DA receptors (which includes D1 and D5) and D2-type receptors (D2, D3, and D4). D1 and D2 represent the vast majority of receptors from their respective families in the rat striatum.[34] All DA receptors are seven-domain transmembrane G-protein coupled receptors with highly conserved sequences.[35] D1 is coupled to G_s and is thus excitatory, while D2 is coupled to G_i and is inhibitory.[34,36] Though some express D1/D2 heterodimers, colocalization is rare and most striatal neurons express either D1 or D2.[34] Presynaptic D2 receptors, when triggered, result in autoinhibition: the state where DA release is suppressed by the interaction of DA in the synaptic cleft binding to the D2 autoreceptor. In this way, DA is capable of regulating its own release. [34,37,38] Raclopride is a selective D2 antagonist used here to lessen the effect of autoinhibition. Raclopride will be used in the experiments described in Chapters 2 and 3.

DA clearance from the extracellular space is accomplished by the DA transporter (DAT). DAT is an integral membrane cotransporter that transports DA back into the cytosol along with two Na^+ ions and one Cl^- ion. The driving force for DA uptake results from ion concentration gradients created by Na^+/K^+ ATPase pumping Na^+ out and K^+ in. The DA is then recycled back

into vesicles by the vesicular monoamine transporter (VMAT). VMAT is located on the membrane of vesicles, and the energy for repackaging is provided by a vacuolar-type H^+ pump ATPase.[36] The competitive DAT inhibitor nomifensine is used in this work to reduce the rate of DA uptake.
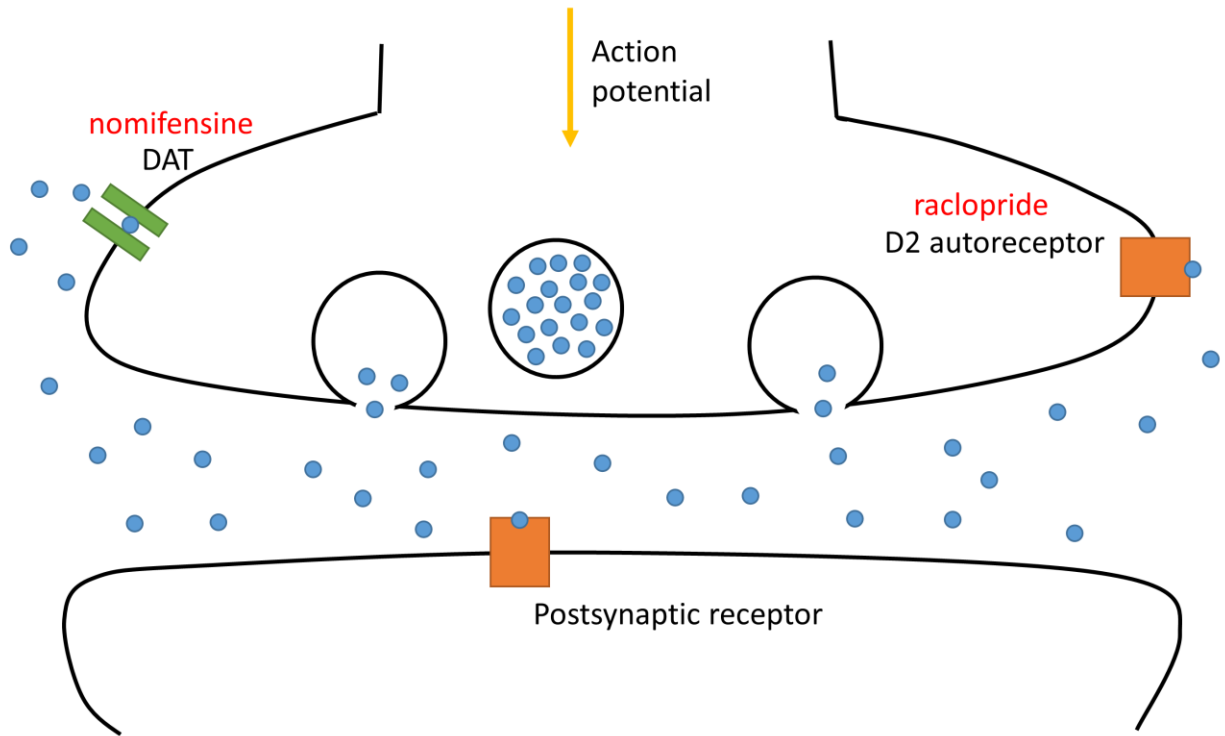

Figure 1-1

A schematic diagram of a DA neuron. Action potentials cause vesicular release of DA (blue dots) into the synapse. From there it binds to pre- or postsynaptic receptors. Raclopride is used in this work to block D2 receptors. DA is reuptaken by DAT where it is repackaged into vesicles. Nomifensine is used here to inhibit DAT.

1.3   FAST SCAN CYCLIC VOLTAMMETRY

DA can be oxidized into dopamine-o-quinone (DAoQ) upon application of a potential above its standard potential. Thus, DA is detected electrochemically with the cyclic voltammetry technique. Cyclic voltammetry offers a unique insight into the molecule being monitored: it allows not only for detection, provides information that can be used to help with molecular identification; this is especially important in an environment as complex as living brain tissue. As the voltage is swept relative to the reference electrode, the shape of the resulting voltammogram reveals characteristics of the molecule generating the current; thus, for a given set of experimental conditions, a molecular "fingerprint" is generated. The oxidation of DA is the result of a two electron, two proton reaction described by the nine membered box scheme.[39] As a result, the rate of the electron transfer reaction is decreased, resulting in a larger peak separation than predicted for an ideal reaction.[40]

The invention of carbon fiber microelectrodes in 1979 by Pujol and coworkers further added to the usefulness of this technique.[41] These microelectrodes have a very small critical dimension (approximately 5-7 µm), allowing for very high spatial resolution, while causing minimal disruption to the normal function of the tissue,[42,43] unlike techniques involving larger implanted devices, such as microdialysis.[14,15,44,45] The additional challenges of microdialysis will be discussed in a later section. Electron microscopy images of carbon fiber electrodes reveal deep ridges, increasing the effective surface area available for electron transfer. The small critical dimensions allow the voltage to be swept at a much faster speed, since the cell time constant is proportional to the electrode radius.[40,46] These high scan rates open the possibility of

sweeping the waveform at frequencies fast enough to measure changes in DA concentration on a physiologically relevant time scale.

An incredible amount of information can be gleaned about a system from FSCV, as the technique provides current versus time plots that can then be converted into concentration over time plots via a simple calibration curve, and voltammograms that through details such as peak height, peak separation, and the overall shape of the curve can provide information about the electrochemical reaction being studied and help identify the molecule. In complex systems such as the brain where multiple analytes may be detected simultaneously and erroneously identified without enough information, this is invaluable. Several molecules present in the brain are oxidized at similar potentials to DA, such as norepinephrine and ascorbate,[41] which can be a challenge to researchers using taking advantage of the incredible temporal resolution afforded by amperometry.[47]

An additional benefit of the use of carbon fiber microelectrodes to detect DA with FSCV involves the adsorption of DA to the electrode surface. The current measured as a result of DA oxidation includes a component resulting from DA that adsorbed to the electrode between scans of the FSCV waveform. Both DA and DAoQ adsorb to carbon fiber electrodes, unique amongst catechols, increasing the current from DA oxidation relative to other contributions to the signal. [38,39] This means that the chosen scan rate and frequency need to be balanced with signal to noise ratio; as the time between scans for DA to adsorb decreases, so does the signal amplitude.[48,49]

However, one drawback of the FSCV method is the very large charging current generated. For potential sweep methods such as cyclic voltammetry, the charging current is directly related to scan rate by the following equation:[40]

Equation 1

$$|i_c| = AC_d v$$

where i_c is charging current, A is electrode area, C_d is the capacitance of the electric double layer, and v is the scan rate. While the peak Faradaic current is related to the square root of the scan rate:

Equation 2

$$i_p = (2.69 \times 10^5)n^{3/2}AD_O^{1/2}C_O^*v^{1/2}$$

Here, i_p is peak current, n is the number of electrons involved in the reaction, D_O is the diffusion coefficient of DA, and C_O^* is the bulk DA concentration. Therefore, as the scan rate increases the charging current increases much more quickly than the Faradaic current. This can be corrected for by removing the charging current contribution to the total signal by background subtraction.[46] A typical trace is shown in Figure 1-2. However, this correction means that it is impossible to measure the basal DA level in the brain with fast scan cyclic voltammetry, only changes in DA levels. All data reported here is background subtracted and zeroed relative to the last voltammetric waveform before the start of the stimulus.

The dimensions of carbon fiber microelectrodes and their relative resistance to breakage make them incredibly powerful sensors for detecting DA in brain slices and even in living animals. The carbon fiber electrode causes very little damage to the surrounding tissue and minimal immune response;[43] thus any recorded responses are from relatively normal, healthy neurons. The carbon fiber working electrode is implanted the striatum, and an Ag/AgCl reference electrode is brought into contact with the surface of the brain with a salt bridge. The

electrical stimulus used in these experiments consists of biphasic constant current square wave 250 µA pulses 2 ms in length delivered at 60, 30, or 15 Hz.
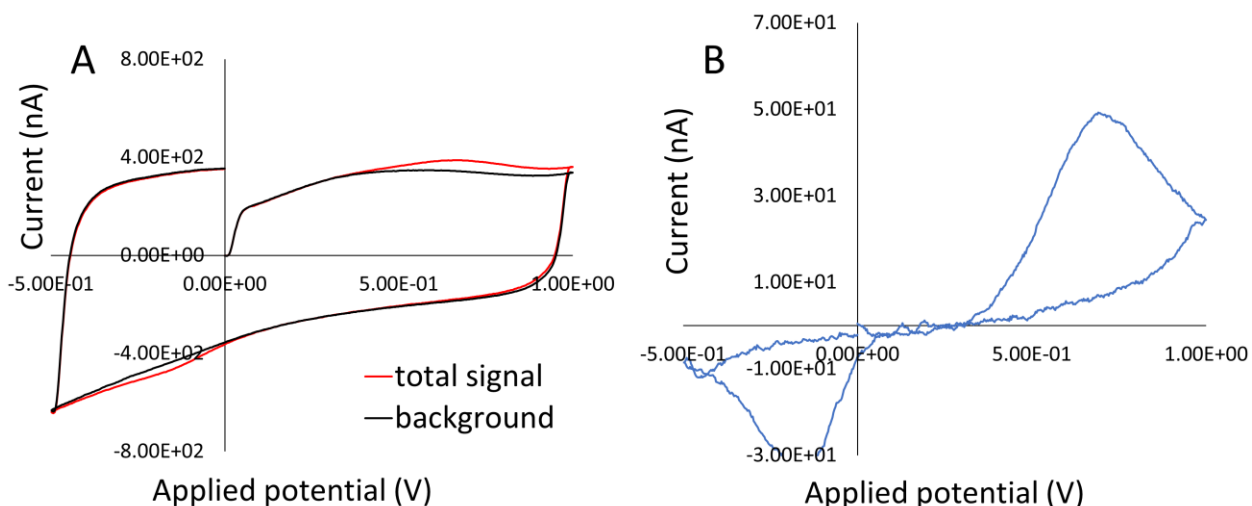
Figure 1-2

Cyclic voltammograms of DA before (A) and after (B) background subtraction. The background charging current (black line) is a very large contributor to the total measured signal (red line) and must be subtracted out, resulting in a visible CV of DA (blue line).

1.4   TRAUMATIC BRAIN INJURY

Traumatic brain injury (TBI) is a significant health crisis across the world. The incidence of TBI in the United States ranges from 180-250 per 100,000 per year, and it is the primary cause of death for individuals younger than 45.[50] TBI is especially dangerous because of numerous complications that can cause the initial injury to expand into the surrounding tissue.[51] After the primary injury caused by the initial trauma occurs, secondary injury resulting from ischemia, elevated intracranial pressure, and cortical spreading depolarization (CSD) and can cause

expansion of the injury lesion into the penumbra – the still alive but endangered tissue surrounding the lesion core.[52–54] CSD in particular is strongly correlated with poor outcome and occur in approximately 60% of TBI patients.[55–57] CSD was first described by Leão in 1944 (then referred to as "spreading depression"), and is a pathological mechanism that disrupts ion gradients across the cell membrane, which require a large amount of energy for repolarization.[58] A metabolic crisis occurs when energy demand exceeds glucose supply, whether due to decreased glucose delivery, such as from ischemia, or increased utilization, like that caused by CSD. This extreme energy demand in an already injured brain can drive the expansion of the injury lesion into the surrounding tissue.[59,60] The ability to monitor for CSDs along with other potentially dangerous disturbances of metabolic homeostasis in real time at the patient's bedside could allow physicians to intervene to prevent injury expansion. To this end, it is important to develop systems to monitor glucose levels in brain tissue in near real time, and simultaneously monitor for CSD; microdialysis coupled to a potassium ion selective electrode (ISE) and a glucose oxidase (GOx)-based glucose electrodes is a perfect candidate for this type of system. Chapter 4 of this document describes a system to monitor glucose and potassium levels in TBI model rats with microdialysis.

1.5   MICRODIALYSIS AND PENETRATION INJURY

Microdialysis is an invasive sampling technique commonly used to monitor small molecules and peptides in the brain in real time.[61–63] Microdialysis has been used since 1972 to monitor molecules in tissues and also for local drug infusion.[64–66] A microdialysis probe consists of an

inlet tube and an outlet tube, connected by a semipermeable membrane. Fluid is perfused through the inlet and into the membrane, where molecules are exchanged between the membrane lumen and the surrounding environment. From there, the fluid is pumped back out through the outlet tube, which can be connected to any number of analysis devices or a fraction collector. Microdialysis is an extremely useful and flexible technique; it can be applied to any molecule that can pass through the membrane and make it to the outlet for detection, and it can be paired with any number of analysis techniques, including high performance liquid chromatography (HPLC)[67,68], mass spectrometry (MS)[69,70] and electrochemical detection.[63,71,72]

The dialysate (i.e., the fluid that has been perfused through the probe) contains a sample of each of the molecules found in the surrounding tissue. The number of molecules exchanged across the membrane is affected by multiple parameters, including flow rate, molecular weight of the analyte, and temperature.[61] In vitro calibrations to control for this cannot be applied to in vivo analyses, because of the inherent tortuosity of the brain and the simple fact that brain tissue is often releasing, removing, and otherwise actively "using" the molecules in the extracellular space.[73,74]

Microdialysis probes are relatively large and inherently perturb the tissue that they are implanted into. While microdialysis probes are well tolerated in a systemic sense, the tissue surrounding the implantation site is disturbed, and there is an immune response to the probe itself that will eventually result in the probe being encased by a glial barrier.[11] While this effect isn't unique to microdialysis, it is particularly crippling; microdialysis probes rely on their ability to exchange molecules with their surroundings. If an impermeable glial barrier forms around the probe, it is effectively useless.

There are several strategies to mitigate the immune response: researchers will wait a certain amount of time after implantation before conducting measurements,[75,76] adjust the implantation location,[77] or repeatedly remove and replace probes.[78] However, our group has had great success by infusing the anti-inflammatory corticosteroid dexamethasone (Dex) into the tissue.[14,45,68,79–81] Histological data shows that Dex infusion prevents the formation of a glial barrier, preserves blood flow to the probe, and protects the surrounding neurons. After five days of Dex retrodialysis (meaning, the infusion of Dex into the tissue through the probe membrane), DA terminals near the probe track responded similarly to electrical stimulation to tissue far from the probe.[81] This effect holds for at least five days after Dex retrodialysis has stopped. Dex retrodialysis opens the door for longer term microdialysis measurements than have ever been possible before.

2.0   DOPAMINE RESPONSE DYNAMICS: KINETICS OR DIFFUSION?

The contents of this chapter have been adapted from Walters, S. H.; Robbins, E. M.; Michael, A. C. Modeling the Kinetic Diversity of Dopamine in the Dorsal Striatum. *ACS Chem. Neurosci.* **2015**, *6* (8), 1468–1475 and Walters, S. H.; Robbins, E. M.; Michael, A. C. The Kinetic Diversity of Striatal Dopamine: Evidence from a Novel Protocol for Voltammetry. *ACS Chem. Neurosci.* **2016**, *7* (5), 662–667.

2.1   INTRODUCTION

Electrically stimulating the MFB results in a release of DA into the striatum. The dynamics of these detected DA responses are highly variable. Previous studies explained this heterogeneity as different densities of DA terminals around recording sites.[33,82,83] The hypothesized variability in terminal density meant that diffusion gaps of different sizes would exist between the terminals and the working electrode. Recording sites that require a relatively long stimulation (greater than 0.2 seconds) for a response to be seen were considered to be locations with a lower terminal density and thus have a larger gap between the terminal and the electrode that DA has to diffuse across before a signal can be seen. Electrode placement was therefore optimized for recording sites that respond quickly to stimulation.

However, evidence now indicates that the heterogeneity is due to kinetics, rather than diffusion. The signals can be organized into statistically distinct groups, broadly categorized as fast and slow responses (Figure 2-1). Fast sites respond immediately to stimulation pulses, while slow sites take at least 0.2 seconds to respond, if not longer.[38] In addition, they respond differently to D2 receptor agonists and antagonists, and to DAT inhibition.[43,84] Interestingly, fast and slow domains also respond differently to stimulations of different frequencies.[12]

As the DAergic system is very complex, controlled by multiple transporters and receptors and resulting in many different and often puzzling downstream physiological effects, it is very attractive to mathematically model evoked DA signals to extract information from the data. Previous models for DA in the striatum have utilized Fick's laws to explain features of the data such as delay and overshoot. Delay is a failure of the stimulus to result in an immediate increase in amplitude and is characteristic of slow sites, while overshoot results from the signal continuing to increase in amplitude after the end of the stimulus and is seen in both fast and slow sites. The diffusion gap model, in various forms, has been used extensively to model evoked DA release, sometimes with the addition of parameters to account for electrode coatings or the formation of biofilms over time.[82,85,86] However, as delay and overshoot are frequently asymmetrical, especially after the application of nomifensine, diffusion across a gap between the neurons and the electrode cannot explain the observed curve shapes.

An alternative explanation for the observation of delay and overshoot has been proposed as restricted diffusion (RD). The RD model, as originally published, is as follows:[16]

Equation 3

$$\frac{dDA_{ic}}{dt} = R_p f e^{-k_R t} - DA_{ic} k_T$$

Equation 4

$$\frac{d[DA]_{oc}}{dt} = \frac{DA_{ic}k_T}{V_{oc}} - [DA]_{oc}k_U$$

The RD model is a set of coupled differential equations that describe the movement of DA released per stimulus pulse, R_p, from the axon terminals to the electrode surface via a first order transport rate k_T, and its subsequent removal from the area around the electrode with a first order uptake rate k_U. The area around the electrode is referred to as the outer compartment, and thus the concentration of DA in the area around the electrode is described by the term $[DA]_{oc}$. V_{oc} is the volume of the outer compartment, and f is the frequency of stimulation. DA_{ic} refers to the amount of DA in the inner compartment: a mathematical construct designed to account for restricted diffusion. Note that the inner compartment is not necessarily an actual physical space; it simply represents something that transports DA to the electrode surface by a first order rate, rather than via the diffusion process as described by Fick's laws of diffusion. Rp, k_U, and k_T are all adjustable parameters, while V_{oc} and f are fixed. The RD model was further refined with the addition of a fourth adjustable parameter, k_R, reflecting changing release over time. Release decays or accelerates exponentially over time, with the rate of decay determined by k_R. The addition of k_R allows the four-parameter version of the RD model to better fit responses, as it better reflects the acceleration/deceleration of the increase in amplitude during the stimulus in slow and fast sites, respectively, than a constant addition of DA does. Figure 2-1B illustrates this difference in release rates.

The experiments described in this chapter sought to measure an upper limit of the distance between the electrode and DA terminals in both fast and slow sites. To this end, rats were given nomifensine, which blocks DA uptake, and raclopride, which prevents autoinhibition,

14

to amplify the signal enough to detect DA overflow resulting from a single stimulus pulse. Animals were then stimulated with a single stimulus pulse. A time gap of varying length was purposefully inserted between the stimulus and the next DA-detecting waveform. A scheme describing stimulus pulse placement relative to FSCV waveform is shown in Figure 2-2.

Additionally, we sought to investigate whether the initial part of fast sites – the first few hundred milliseconds that are most distinct from slow sites – operate under the same kinetics as slow sites. To that end, we gave rats nomifensine and raclopride and applied 1 through 6 stimulus pulses and modeled the results with the same RD model that we have had success with in slow sites and the later component of fast sites.
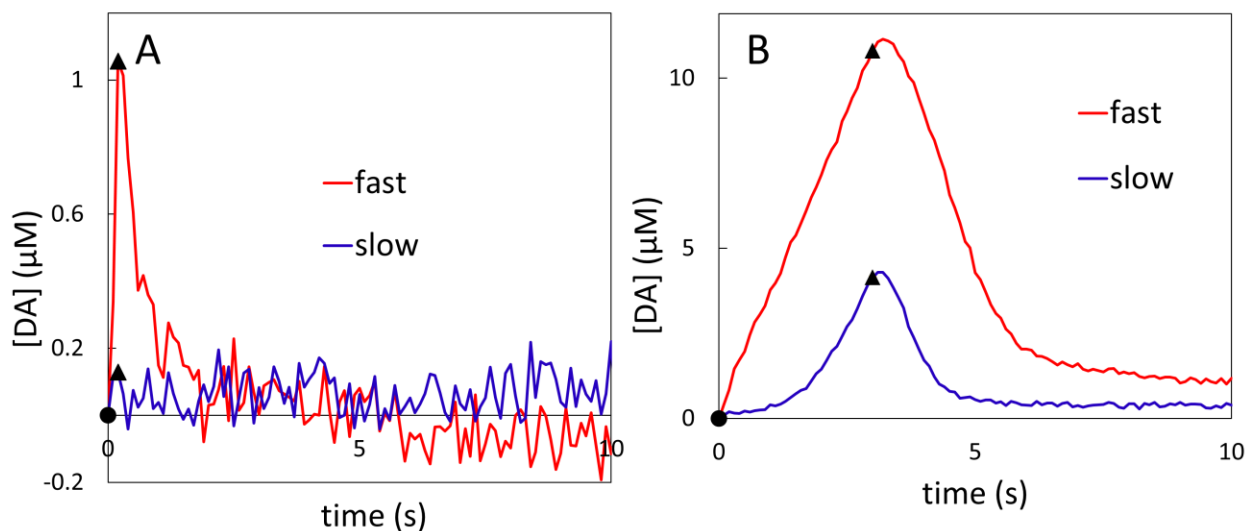
Figure 2-1

A) Fast sites (red) are identified by their response to a 0.2 s stimulation. Slow sites (blue) do not respond. Circles indicate stimulus start while triangles are the end of the stimulation. B) Fast sites respond immediately to stimulation, while slow sites take longer and tend to have an accelerating pattern of release.
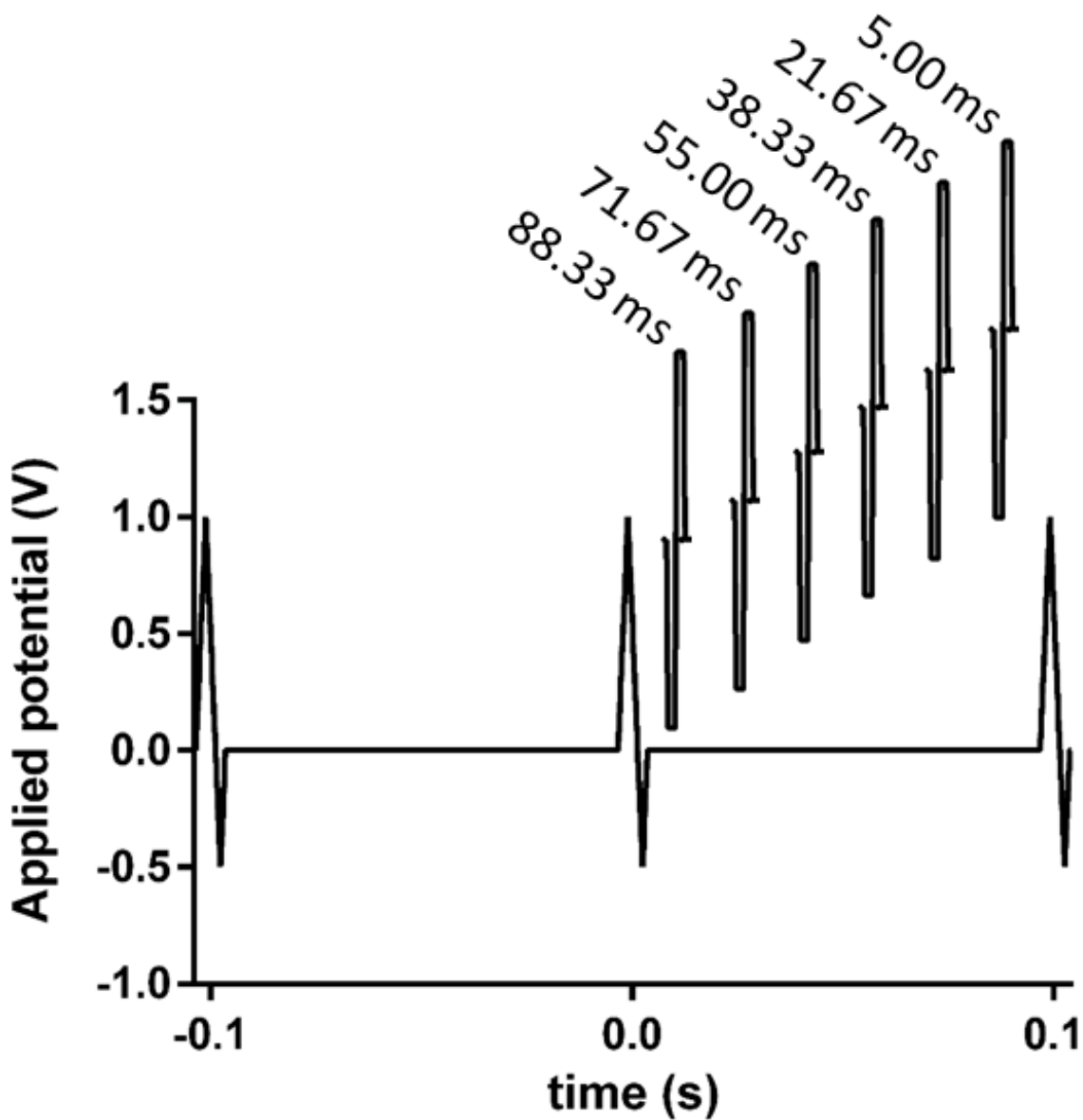
Figure 2-2

Experiment scheme. Varying time gaps are placed in between the stimulus pulse and the first voltammetric waveform after the stimulus at 0.1 s. Time gaps vary from 5.00 ms to 88.33 ms at 60 Hz intervals. The gap time is calculated as the time in between the start of the stimulus pulse and the start of the voltammetric waveform.

2.2 METHODS

2.2.1 FSCV procedures

Carbon fiber electrodes (T650 fibers, Cytec LLC, Piedmont, SC, USA) 7 µm in diameter were inserted into a borosilicate glass capillary and pulled to a sharp tip. The carbon fibers were then sealed in place with epoxy and cut to a length of 200 µm. The FSCV waveform had a rest potential of 0 V, a positive limit of 1 V, a negative limit of -0.5 V (all vs Ag/AgCl), a sweep rate of 400 V/s, and a repetition frequency of 10 Hz. In vitro FSCV calibration was performed in a homemade flow cell attached to a Rheodyne loop-style low-pressure sample injector valve. Flow was generated by hydrostatic pressure from an elevated reservoir containing N_2-purged artificial cerebrospinal fluid (142 mM NaCl, 1.2 mM $CaCl_2$, 2.7 mM KCl, 1.0 mM $MgCl_2$, 2.0 mM NaH_2PO_4, pH 7.4).

2.2.2 Animal procedures

All procedures involving animals were carried out with the approval of the University of Pittsburgh Animal Care and Use Committee. Rats (male, Sprague−Dawley, 250−350 g, Charles River Inc., Wilmington, MA) were anesthetized with isoflurane (2.5% by volume O_2), placed in a stereotaxic frame (David Kopf, Tujunga, CA), and connected to an isothermal blanket (Harvard Apparatus, Holliston, MA). Carbon fiber electrodes and stimulating electrodes (MS303/a, Plastics One, Roanoke, VA) were implanted in the DS and ipsilateral medial forebrain bundle, respectively. Optimization was performed to identify recording sites that produce fast-type

evoked responses. The experimental stimulus waveform was a biphasic constant current square wave (2 ms pulses, 60 Hz, 250 µA, 1−6 pulses) delivered with a stimulus isolation unit (Neurolog 800, Digitimer, Letchworth Garden City, UK). Responses evoked by single stimulus pulses were recorded in n = 14 rats treated first with nomifensine (20 mg/kg ip) and then 20 min later with raclopride (2 mg/kg i.p.): in 7 of these rats recordings were taken at fast sites and in the other 7 rats recordings were taken at slow sites. The time between the single stimulus pulse and the subsequent FSCV scan was varied in increments of 16.67 ms, the period of a 60 Hz stimulus (see Figure 2-2).

2.2.3   Curve fitting

Curve fitting was used to set the values of the adjustable parameters in the RD model. In each case, a search was conducted for those parameters that produced the best fit between the models and target data as defined by the smallest accessible sum of squares of the residuals. The overall quality of the best-fit model was assessed by means of the Pearson correlation coefficient. The search algorithm was a brute force procedure described in detail in other publications.[16–18]

2.3   RESULTS AND DISCUSSION

2.3.1   Measuring the distance between terminals and the electrode

An experiment was devised in which a single stimulus pulse was applied to both kinetic fast and slow sites, but the length of time between the pulse and the next application of the data-

18

collecting waveform was varied at 60 Hz time intervals. These rats were treated with the DAT inhibitor nomifensine (20 mg/kg, i.p.) and the D2 antagonist raclopride (2 mg/kg, i.p.), lessening the effects of uptake and autoinhibition, to amplify the signal enough to visualize the response to single pulse stimulations. In this way, a time delay between the stimulus and the voltammetric waveform was purposefully inserted. Fast responses are shown in Figure 2-3. The concentration of DA measured at the first waveform after the stimulus was analyzed for statistical significance, shown zoomed in Figure 2-3B. Stimulus pulses applied with a 55.00 ms or greater time gap before the waveform result in a statistically nonzero response in slow sites (Figure 2-4, blue bars, 1-tailed t-test, $p < 0.05$, n=7 rats) and 38.33 ms or greater in fast sites (Figure 2-4, red bars, 1-tailed t-test, $p < 0.05$, n=7 rats). This time delay corresponds to a maximum gap size of 3.6 μm in slow sites and 3.0 μm in fast sites. Linear diffusion across a gap this small cannot explain the long delays observed in kinetic slow sites without nomifensine and raclopride treatment. Distances were calculated with the following equation:

Equation 5

$$gap\ size = \sqrt{Dt}$$

where D is the diffusion coefficient of DA in the striatum, 2.4 x 10^{-6} cm^2/s,[87] and t is the time in seconds. Calculated gap sizes should be treated as an upper limit, as linear diffusion is assumed here with nothing in between the electrode and the axon terminal. The gap sizes agree well with the average distance between DAergic axon terminals in the DS.[32]

Figure 2-3

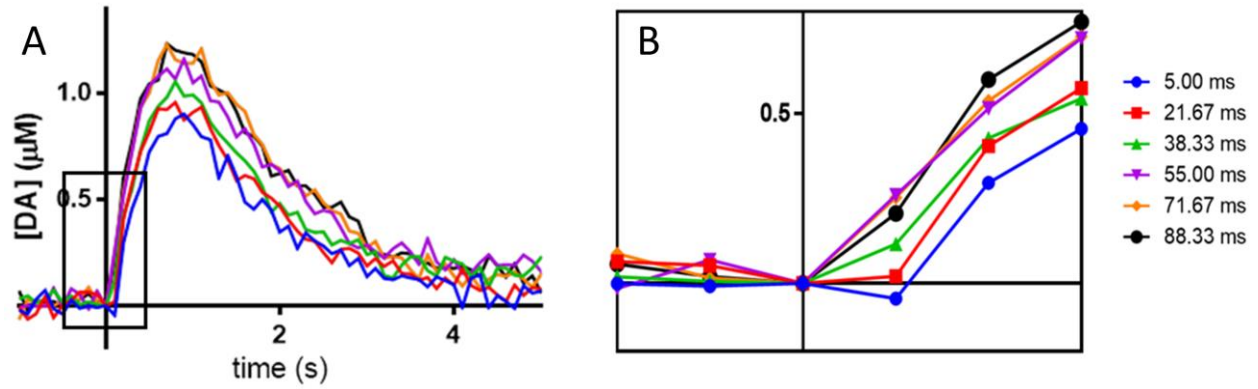Responses evoked by a single stimulus pulse applied at different times relative to the FSCV waveform in n = 7 fast sites. Rats were treated with nomifensine and raclopride. The DA concentration at the 100 ms data point (shown in detail in panel B) are examined further to estimate an upper limit on the distance between the working electrode and the DA-releasing axon terminals.
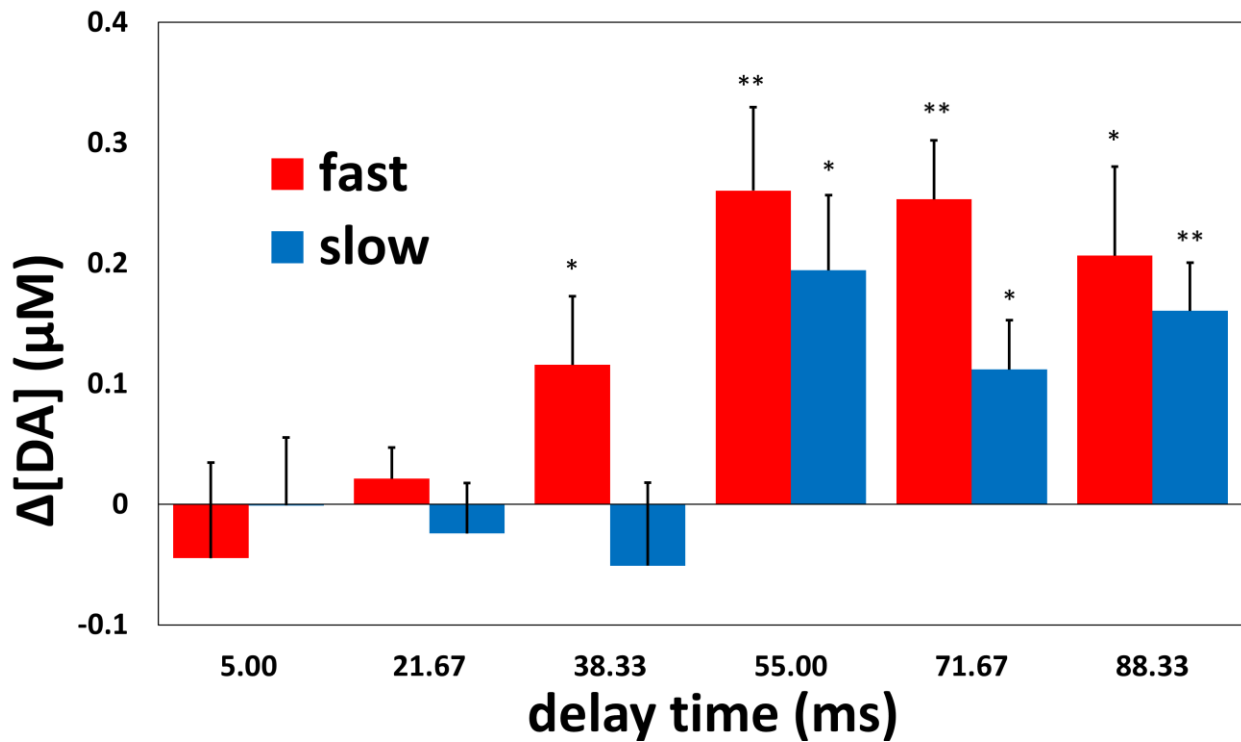

Figure 2-4

20

The amplitude of DA response at 0.1 s as a function of the delay time (mean ± SEM). In fast sites, DA reaches a statistically significant amplitude above zero at delay times above 38.33 ms (one-tailed t test: $t(6) = 2.036$, $p < 0.05$), while slow domains reach a significant amplitude at delay times of 55.00 ms or greater (one-tailed t test: $t(6) = 3.116$, $p < 0.05$).

2.3.2 Kinetics of the fast initial component

If fast and slow sites are not due to a large difference in the distance between the electrode and the DA terminals, they must be due to kinetics. Because we have previously shown that the RD model can fit slow sites very well in their entirety, but it struggles to fit the initial few data points of fast sites,[17] we postulate that slow sites and the later portion of fast sites operate under similar kinetic rules, but fast sites have an additional "fast initial component."

To investigate whether or not this fast initial component operates under the same kinetics as the slower component, just at a different timescale, we recorded responses evoked by 1 to 6 individual stimulus pulses in 10 nomifensine treated rats. First, we modeled each response individually (Figure 2-5A: these fits are excellent but the Pearson correlation coefficients are ~0.96 due to the residual noise). In this case, we set k_R to zero as it had no obvious effect on the quality of the fits, so the fits in Figure 2-5A were obtained with a 3-parameter version of the model. Second, we modeled all six responses simultaneously (Figure 2-5B: the fit is again excellent but the correlation coefficient is also ~0.96 due to residual noise). Thus, Figure 2-5A shows that the individual responses can each be fit with 3 adjustable parameters and Figure 2-5B shows that the entire data set can be modeled with a single set of the 4 adjustable parameters. The parameters of the fits are reported in Table 2-1 in the Supporting Information section of this chapter.

21

Figure 2-5 confirms that the brief stimulus responses exhibit the same overall kinetic behaviors as the prolonged responses in Figure 2-1B. Previous publications have shown the model fits the slow component of stimulations; only the numerical values of the adjustable parameters are different between the slow and fast components. The k_T values fall in the consistent $1-2$ s^{-1} range; this is in line with previously published RD model results.[16,17] The k_U values are smaller than k_T, an expected consequence of nomifensine administration. The R_P values are ~10-fold larger than those obtained by modeling the prolonged responses. There may be two reasons for this: first, the responses predominantly represent the initial fast component, and second, uptake inhibition mobilizes DA vesicle pools and promotes DA release.[88].
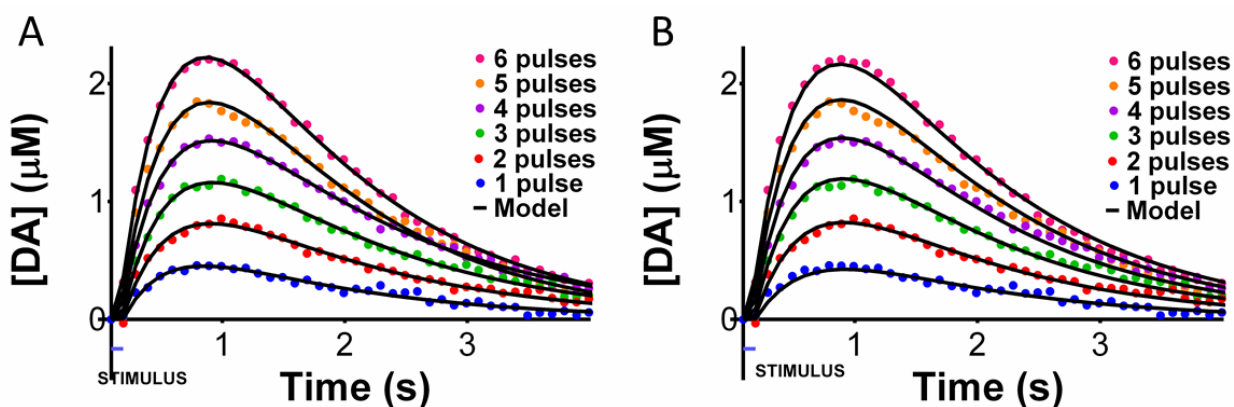
Figure 2-5

Symbols: Fast responses evoked by 1-6 stimulus pulses in rats (mean of n=10, SEMs omitted for clarity) treated with nomifensine (20 mg/kg i.p.). Lines: Best-fit models. (A) Best-fit models to each evoked response. (B) The single best-fit model to all six evoked responses.

2.4   CONCLUSIONS

Together with previous reports the work in this chapter establishes that fast and slow DA response patterns are kinetic phenomena. Slow sites are not the result of poor electrode placement, as has been previously thought. Slow sites are "real" responses stemming from differences in release, transport, and uptake of DA across the striatum. Additionally, slow sites and the initial fast component can both be fit with very high fidelity by the RD model, meaning that they operate under the same kinetics, just at a different timescale. Chapter 3, next, explores the underlying cause of fast and slow kinetic sites.

2.5   SUPPORTING INFORMATION

Table 2-1

	R_P (mol)	k_U (s^{-1})	k_T (s^{-1})	k_R (s^{-1})
Figure 2-5A, 1 pulse	1.2E-20	0.71	2.8	
Figure 2-5A, 2 pulses	1.1E-20	0.67	2.5	
Figure 2-5A, 3 pulses	1.0E-20	0.67	2.3	
Figure 2-5A, 4 pulses	1.0E-20	0.64	2.4	
Figure 2-5A, 5 pulses	1.1E-20	0.82	2.1	
Figure 2-5A, 6 pulses	1.0E-20	0.77	2.3	
Figure 2-5B	1.2E-20	0.73	2.3	4.1

Parameter values for the fits shown in Figure 2-5.

3.0 THE ROLE OF AUTOINHIBITION IN FAST AND SLOW DOPAMINE RESPONSES

3.1 INTRODUCTION

As discussed in Chapters 1 and 2, the combination of in vivo FSCV, carbon fiber microelectrodes, and electrical stimulation of DA neurons or axons has proven useful for assessing DA release and clearance in the DS, VS, and other terminal fields in living animals and in slice preparations.[89–93] Electrically evoked DA responses exhibit temporally fine details that reflect the diversity of the kinetics of DA release and clearance. Numerical modeling is one approach to evaluating these fine details in terms of the rates and rate constants of DA release, mass transport in the extracellular space, adsorption of DA to carbon fiber microelectrodes, and DA uptake via the dopamine transporter.[16,18,85,94,95]

The previous chapter described an RD model that reproduces 5 different types of evoked response (4 fast subtypes and 1 slow type) from the DS,[96] and two types (fast and slow) from the VS, of the rat.[16,97] In addition to the rise, fall, and amplitude of the responses, the model reproduces the delays that occur when the stimulus begins and ends, known colloquially as lag and overshoot, respectively.[16–18] The RD model produces high fidelity fits (i.e. $r^2 > 0.99$) to responses recorded over a variety of stimulus conditions before and after systemic administration of the DA uptake inhibitor, nomifensine.

The experiments in this chapter apply new versions of the RD model to responses recorded over a wider range of stimulus durations (60, 180, and 600 pulses) and frequencies (15, 30, and 60 Hz) before and after the systemic administration of the D2 receptor antagonist, raclopride. A specific objective was to test the hypothesis that the unique features of fast and slow responses from the DS are attributable to autoinhibition. The wider range of experimental conditions required modifications of the original RD model. As a result, model parameters became harder to compare between experimental conditions, because some parameters are no longer equivalent to each other between different versions of the RD model. Therefore, we developed the concept of a delivery curve to graphically represent the combined rate of DA release and transport to the FSCV electrode. Finally, this chapter explores in more detail the issue that the model sometimes finds more than one set of best-fit parameters for an individual response.

3.2   METHODS

3.2.1   FSCV procedures

FSCV procedures are identical to those described previously in other publications and in Chapter 2 of this document.[43,98,99] A carbon fiber (7 µm in diameter, T650 fibers, Cytec LLC, Piedmont, SC, USA) was sealed with epoxy (Spurr, Polysciences, Warrington, PA, USA) into a pulled borosilicate capillary (Sutter Instrument, Novato, CA, USA). The exposed fiber was cut to a length of 200-250 µm. The FSCV waveform (0 V to 1 V to -0.5 V to 0 V vs. Ag/AgCl at 400

V/s) was repeated every 100 ms. The microelectrodes were post-calibrated in vitro in a flow cell gravity fed with N_2-purged artificial cerebral spinal fluid (aCSF: 145 mM NaCl, 2.7 mM KCl, 1.2 mM CaCl2, 2.0 mM phosphate, pH 7.4). Standards for calibration were prepared by dissolving dopamine hydrochloride (Sigma Aldrich, St. Louis, MO) in aCSF. Fast and slow locations were determined by performing a 60 Hz, 12 pulse stimulation. If the site responded, it was determined to be fast. Otherwise, it was classified as slow.

3.2.2   Animal procedures

Again, the University of Pittsburgh Institutional Animal Care and Use Committee approved all procedures involving animals. Male Sprague-Dawley rats (250-350 g, Charles River Inc., Wilmington, MA) were anesthetized with isoflurane (2.5% by volume O_2) and placed in a stereotaxic frame (Kopf, Tujunga, CA, USA) under an isothermal blanket (Harvard Apparatus, Holliston, MA, USA). The carbon fiber electrode was inserted into the DS (from bregma: 3.8 mm lateral, 0.2 mm anterior, 4.5 mm below dura), the stimulating electrode (MS303/a, Plastics One, Roanoke, VA, USA) was lowered into the ipsilateral MFB (from midline: 1.2 mm lateral, from bregma: 4.3 mm posterior, 7.2 mm below dura), and a Ag/AgCl reference electrode was placed in contact with the contralateral cortex. A stimulus isolation unit (Neurolog 800, Digitimer, Letchworth Garden City, UK) delivered biphasic, constant current stimulus pulses with a duration of 2 ms and amplitude of 250 µA. Stimulus frequency and duration were variable and are specified in the Results and Discussion section. Post-raclopride (2 mg/kg i.p.) data were recorded 20 minutes after drug administration. Evoked responses reported in the figures are the

mean of at least n=5 individual responses from different rats: all responses were processed with the hang-up removal algorithm described by Walters et al.[16]

3.2.3 The restricted diffusion (RD) model

As described in the previous chapter, the RD model postulates that the extracellular space is divided into inner and outer compartments and that DA is released into the inner compartment, undergoes restricted diffusion to the outer compartment, and is removed from the outer compartment by uptake. The time-varying concentration of DA in the outer compartment represents the DA concentration measured via FSCV. Curve fitting procedures were identical to those in Chapter 2.

This work involves several versions of RD model, to which we assign unique names for clarity of discussion. The original model, here called RD-1 refers to Equation 3 and Equation 4 from the previous chapter. An objective search algorithm is used to find the set of parameters (R_p, k_R, k_T, and k_U) that produces the smallest sum of squared residuals. The quality of the fit is assessed with Pearson's correlation coefficient, r^2: our target during this study was $r^2 > 0.99$, which indicates excellent agreement between the model and the data. From the initial conditions that $DA_{ic} = 0$ and $[DA]_{oc} = 0$, a finite elements routine generates values of $[DA]_{oc}$ over time.

3.2.4 Modified RD models

Other versions of the RD model are listed here. RD-2 has an additional parameter to modulate DA release:

RD-2:

Equation 6

$$\frac{dDA_{ic}}{dt} = R_p f(e^{-k_{R1}t} - e^{-k_{R2}t}) - DA_{ic}k_T$$

where t is time, DA_{ic} is the amount of DA in the inner compartment, $[DA]_{oc}$ is the concentration of DA in the outer compartment, R_p is an initial value for moles of DA released per stimulus pulse, f is the frequency of the stimulus pulses, k_{R1} and k_{R2} modulate the amount of DA released per pulse (allows DA released per pulse to vary with time), k_T is the first order rate constant for transport to the outer compartment, V_{oc} is a volume element of the outer compartment, and k_U is the first order rate constant for uptake.

RD-3 also has an additional parameter to modulate DA uptake, k_{U2}:

RD-3:

Equation 7

$$\frac{dDA_{ic}}{dt} = R_p f(e^{-k_{R1}t} - e^{-k_{R2}t}) - DA_{ic}k_T$$

Equation 8

$$\frac{d[DA]_{oc}}{dt} = \frac{DA_{ic}k_T}{V_{oc}} - [DA]_{oc}k_U e^{-k_{U2}t}$$

RD-4 is adapted to simulate cases of "extreme lag" observed at the lower stimulus frequencies, 15 and 30 Hz:

RD-4:

Equation 9

$$\frac{dDA_{ic}}{dt} = R_p f \frac{\theta}{1+\theta} e^{-k_R t} - DA_{ic}k_T$$

where $\theta = \exp(k(t - \tau))$.

3.2.5 Delivery curves

A new strategy was needed to combine and compare modeled results obtained with different versions of the RD model. This is because the modifications change the mathematical meaning of the various parameters, especially R_p and k_U, such they are not directly comparable to each other. However, all 4 versions of the model use the same expression to describe the rate at which DA is transported from the inner to the outer compartment (the first term on the righthand side of Equation 3, Equation 6, Equation 7, and Equation 9):

Equation 10

$$\frac{d[DA]_{oc,d}}{dt} = \frac{DA_{ic}k_T}{V_{oc}}$$

hence, it is practical to compare delivery curves obtained with the different models, where delivery is defined as:

Equation 11

$$\Delta[DA]_{oc,d} = [DA]_{ic} \cdot k_T \cdot \Delta t$$

where $[DA]_{ic} = DA_{ic}/V_{oc}$ and Δt is the length of the time steps in the finite elements routine. Essentially, $\Delta[DA]_{oc,d}$ is the change in the concentration of DA in the outer compartment during each time iteration due to the combined contributions of DA release into, and transport out of, the inner compartment.

3.2.6 Clearance curves

Clearance curves are obtained in the same manner as the delivery curves while using the 2nd term on the righthand side of Equation 4 and Equation 8. It is important to note that the clearance curves are not independent of the delivery curves: for example, increased delivery leads to increased clearance simply by virtue of the higher concentration of substrate. Both the delivery and clearance curves reflect the coupled rates of the delivery and clearance processes, not their independent rate constants.

3.2.7 Finding the local minima

To find all the local minima that the model could produce, we selected a reasonable range for each parameter and simulated a curve for every combination of those parameters. We compared each simulation with a sample data set and calculated an SSR. For simplicity, Figure 3-7b is a plot of just the minimum SSR found for each Rp value in the selected range. A figure showing each of the two best fits vs k_U and k_T is shown in the Supporting Information section of this chapter, in Figure 3-11.

3.3   RESULTS AND DISCUSSION

3.3.1   Models of fast and slow sites, pre- and post-raclopride

Figure 3-1 compares the RD model to slow type (Figure 3-1a) and fast type (Figure 3-1c) evoked DA responses from the DS prior to raclopride administration during 60-Hz stimuli of 60, 180, and 600 pulses. To obtain Figure 3-1, each evoked response was modelled individually. In the case of slow sites, the original 4-parameter RD model, herein called the RD-1 model, produced good fits to the 60 and 180-pulse responses. However, the RD-1 model was unable to fit the 600-pulse stimulus response, which reaches a maximum and then declines before the stimulus ends. The RD-2 model, with one additional parameter, produced an excellent fit. In the case of fast sites, the RD-1 model produced excellent fits to 60 and 180-pulse response and the RD-2 model produced an excellent fit to the 600-pulse response. However, consistent with our previous experience, it was necessary to add an initial fast release component to account for the leading shoulder that is the hallmark of the fast-type responses.[17] The fits to the data and all associated parameter sets are located in the Supporting Information section of this chapter.

Figure 3-1b and d show slow and fast responses, respectively, recorded after the systemic administration of raclopride. The RD-1 model produced excellent fits to all the post-raclopride responses: neither the RD-2 model nor the initial fast component was needed to fit these data. In that respect, one effect of raclopride administration is to simplify the dynamics of evoked DA responses.

Figure 3-1 shows that the RD model(s) provide excellent fits to the various individual evoked responses. However, these individual fits are not convenient for analyzing raclopride's

mechanism of action on the evoked responses. First, each response has its own unique set of best-fit parameters, so it is not possible to assign specific pre- and post-raclopride parameter values. Second, the individual fits required 3 different models (RD-1, RD-2, and the initial fast component): when different models are used in this way, the parameter values cannot be directly compared.

In order to proceed with the analysis of the effects of raclopride, we modeled each set of evoked responses (60, 180, and 600 pulses) as a single data set (Figure 3-2). This approach produced a single set of best-fit parameters for each of the four experimental conditions (fast and slow, pre and post). We used the RD-3 model, with 6 adjustable parameters, because neither the RD-1 nor the RD-2 models were able to reach the $r^2 > 0.99$ target. As with Figure 3-1, the fast pre-raclopride responses also required the additional fast initial release component. Figure 3-2 shows some differences between the modeled and measured responses, especially the declining phase of the 60-pulse responses. This occurs because the 60-pulse responses make the smallest contributions to the sum of squared residuals, hence the optimization procedure places more weight on the larger-amplitude, longer-duration responses. The model provides an excellent fit to the rising phase of the response, which bodes well for investigating the effects of raclopride on DA release.

Figure 3-3 shows the delivery curves for the simulations in Figure 3-2. In the case of slow responses, Figure 3a indicates that raclopride increased DA delivery from the very beginning of the stimulus. This suggests that raclopride acts to block an underlying autoinhibitory tone that exists even prior to the onset of the stimulus. In the case of the fast responses, Figure 3-3b indicates that raclopride had no effect on DA delivery during the first 500-700 ms of the stimulus, which suggests the absence of an autoinhibitory tone. Raclopride,

however, increased DA delivery once the stimulus itself increased extracellular DA, presumably to a concentration able to compete with raclopride. Overall, the model supports the conclusion that slow and fast sites correspond to striatal locations with and without autoinhibitory tone, respectively.

It is quite noticeable in Figure 3-3a and b that raclopride administration caused DA delivery to reach a maximum sooner. It seems likely that the maximum in delivery reflects the availability of DA for release, possibly determined by the size of the releasable pool. Thus, Figure 3-3 suggests that the releasable pool is depleted more rapidly in the presence of raclopride. To compare the temporal details of the fast and slow post-raclopride delivery curves, they are re-plotted together in Figure 3-3c, normalized to their respective maximum values. The temporal dynamics of the delivery curves are essentially identical. Thus, Figure 3-3c lends strong support for the conclusion that D2 autoreceptors play a major role in determining the distinct temporal features of the fast and slow delivery curves: under these stimulus conditions, raclopride completely abolishes such distinctions.
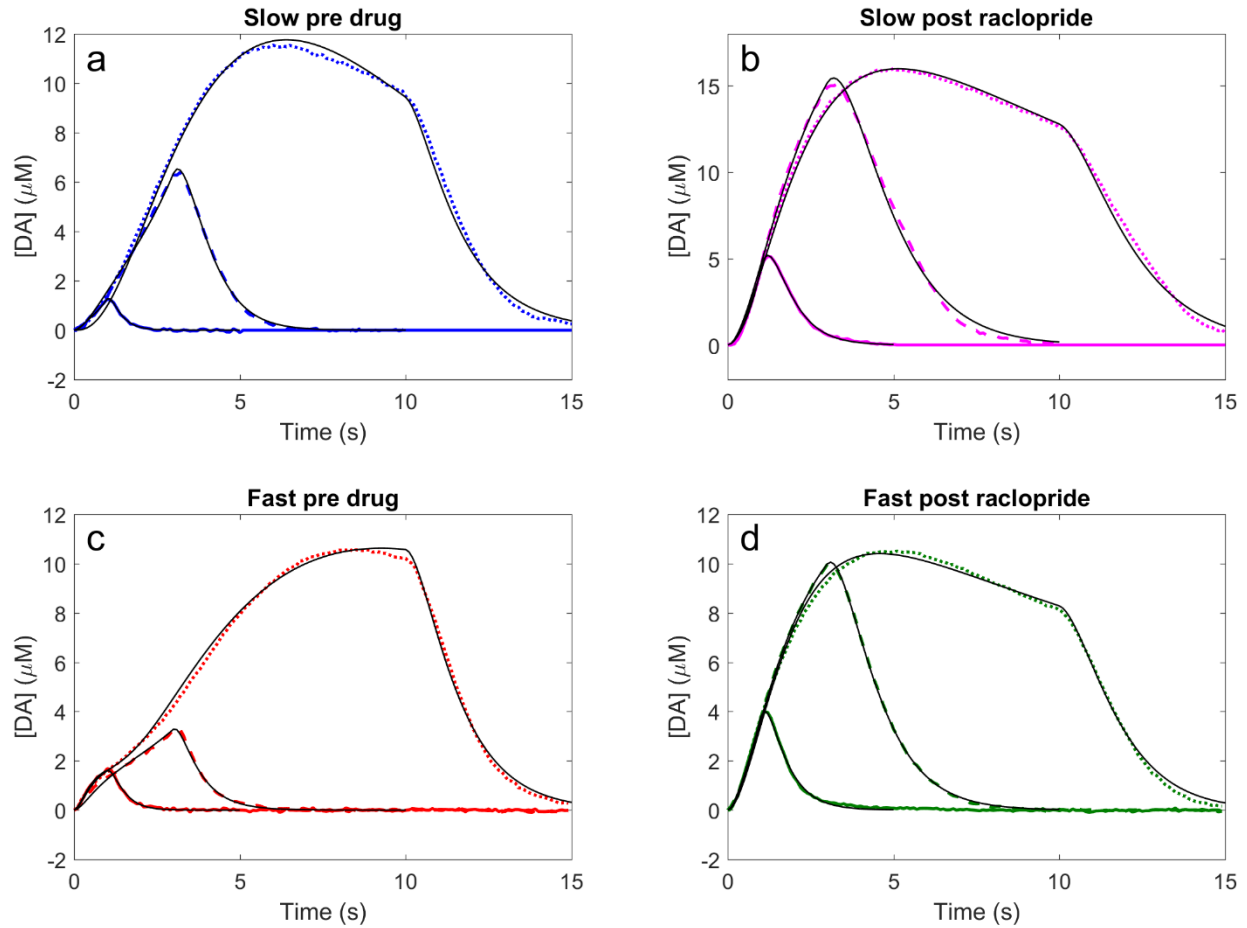
Figure 3-1

Plots of 60 Hz stimulations of 60 pulses (solid colored lines), 180 pulses (dashed lines), and 600 pulses (dotted lines) in length. All model fits are shown in black. The RD model can reproduce slow pre-drug data (a, blue), slow post-raclopride data (b, purple), fast pre-drug data (c, red) and fast post-raclopride (d, green). All data except the pre drug 600 pulse stimulations were able to use the RD-1 model. Those two stimulations were a special case requiring the RD-2 model.

Figure 3-2

Data from 60 (solid colored lines), 180 (dashed lines) and 600 (dotted lines) pulse stimulations in slow sites, pre (a, blue) and post (b, purple) raclopride and in fast sites, again both pre- (c, red) and post- (d, green) raclopride modeled with the RD-3 model. In each panel, all three stimulation lengths were fit to the same 6 parameters.
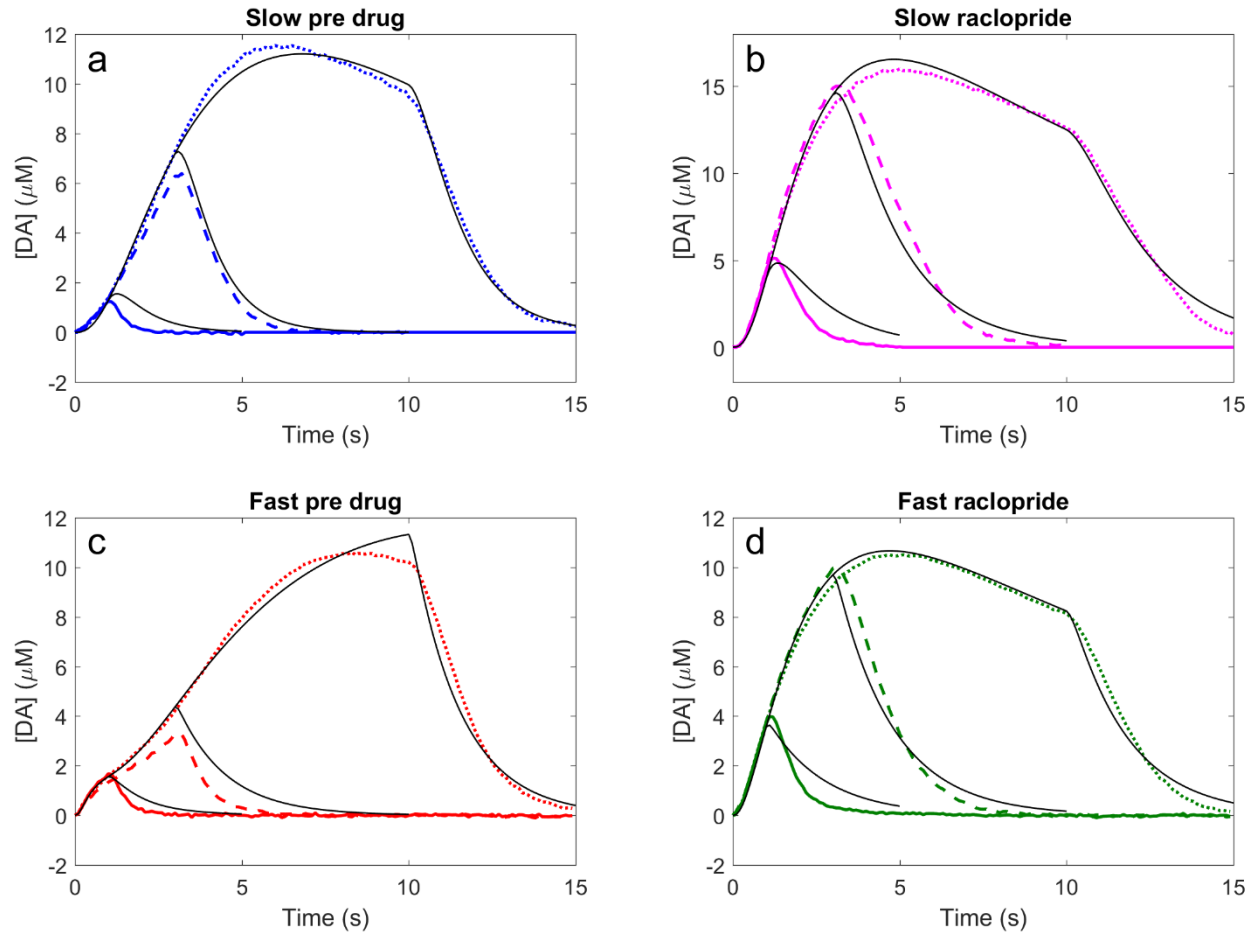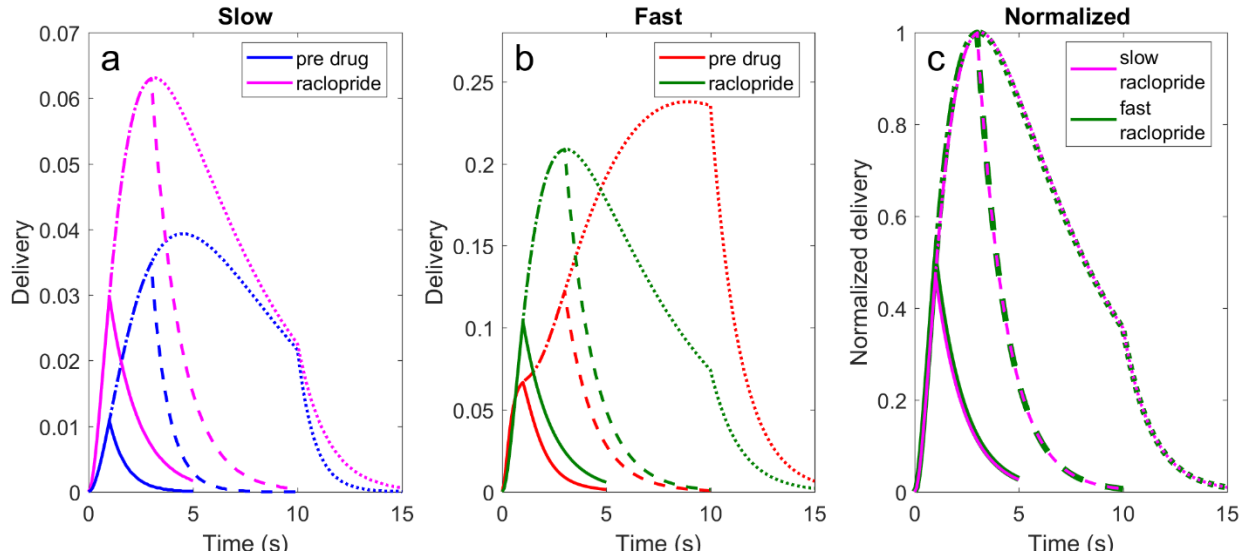
Figure 3-3

Delivery curves for 60 pulse (solid lines), 180 pulse (dashed lines), and 600 pulse (dotted lines) stimulations in fast and slow sites before and after raclopride administration. a) Slow sites display an immediate increase in delivery after raclopride (purple) when compared to the pre-drug response (blue). b) Fast sites, however, show little change in delivery after raclopride administration (green) compared to the pre drug response (red) for the first 500-700 ms. c) Normalized slow (purple) and fast (green) sites have the same delivery response shape after raclopride administration.

3.3.2 Different effects of raclopride with low frequency stimulations

We modeled pre- and post-raclopride responses evoked by 60, 180, and 600 pulses at frequencies of 15 and 30 Hz. We again modeled responses under each condition (fast and slow, pre and post) as a single data set. The RD-4 model, also with 6 adjustable parameters, was necessary to achieve the target of $r^2 > 0.99$: a fast initial component was not needed. Figure 3-4 shows the normalized delivery curves obtained from these simulations. At slow sites, raclopride altered the

36

amplitude and temporal details of the delivery curves (Figure 3-4a and b), as was the case at 60 Hz (Figure 3-3a). At fast sites, however, the shapes of the pre- and post-raclopride normalized delivery curves are quite similar (Figure 3-4c and d). Thus, at these lower frequencies raclopride altered the amplitude, but not the shape, of the delivery curve, in contrast to what we observed at 60 Hz (Figure 3-3b). Moreover, at these lower frequencies, the post-raclopride slow and fast delivery curves did not show the essentially identical character that we observed at 60 Hz (Figure 3-3c). Overall, the actions of raclopride on the DA delivery curves depend on both the nature of the site (fast and slow) and the stimulus frequency.
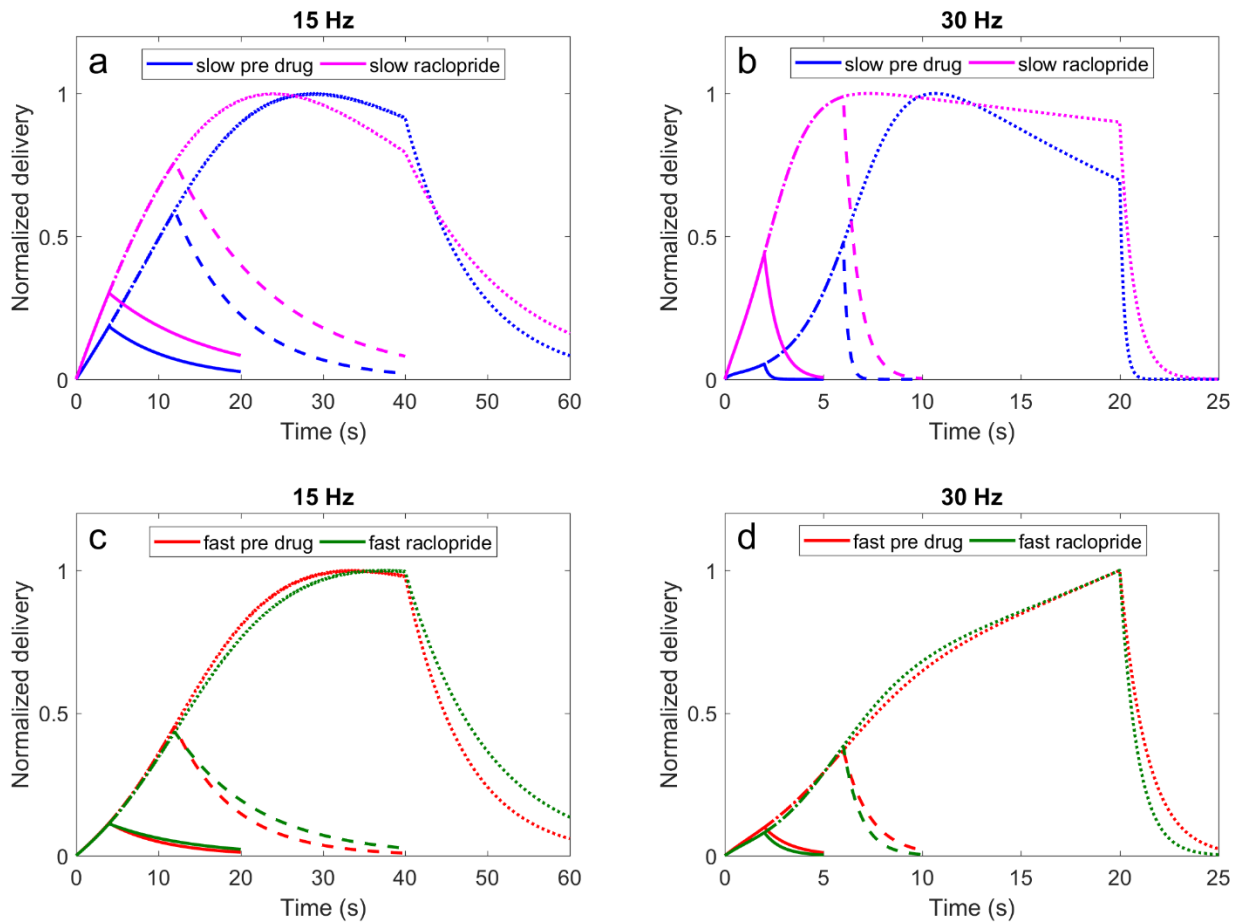

Figure 3-4

Normalized delivery curves from slow (a and b) and fast (c and d) sites obtained at stimulus frequencies of 15 (a and c) and 30 Hz (b and d). Pre-raclopride responses are in blue and red. Post-raclopride responses in pink and green. Raclopride alters the amplitude of delivery in slow and fast sites. Raclopride alters the temporal dynamics of delivery in slow sites but not in fast sites.

3.3.3   Conversion of fast to slow evoked DA behavior

The clearest contrast between the actions of raclopride in fast and slow sites occurs during the initial stages of the stimulus at 60 Hz. We elected to examine this phenomenon in more detail by inspecting both DA release and clearance curves obtained from 60-Hz, 60-pulse responses under the four experimental conditions (fast and slow, pre and post raclopride). Since the stimulus is relatively brief, the 4-parameter RD-1 model was sufficient to achieve the target of $r^2 > 0.99$.

As reported above, raclopride had relatively little effect on the delivery curve in fast sites (Figure 3-5b). However, raclopride decreased the amplitude of the fast-site clearance curve (Figure 3-5d). As explained in the Methods section of this chapter, clearance is not independent of delivery: increased delivery generates more substrate for clearance. In this case, however, raclopride decreased clearance without decreasing delivery, showing that raclopride slowed the rate and the kinetics of clearance. In slow sites, raclopride increased DA delivery (Figure 3-5a) but not DA clearance (Figure 3-5c). Since there was no increase in clearance rate, despite the increase in delivery rate, raclopride also slowed the kinetics of DA clearance in slow sites. This observation is consistent with numerous previous reports that DA clearance is under the influence of D2 autoreceptors.[84,100,101] However, in the case of fast sites, raclopride's tendency to decrease DA clearance without affecting DA delivery comes as a surprise. We can speculate that different populations of D2 receptors might be involved.
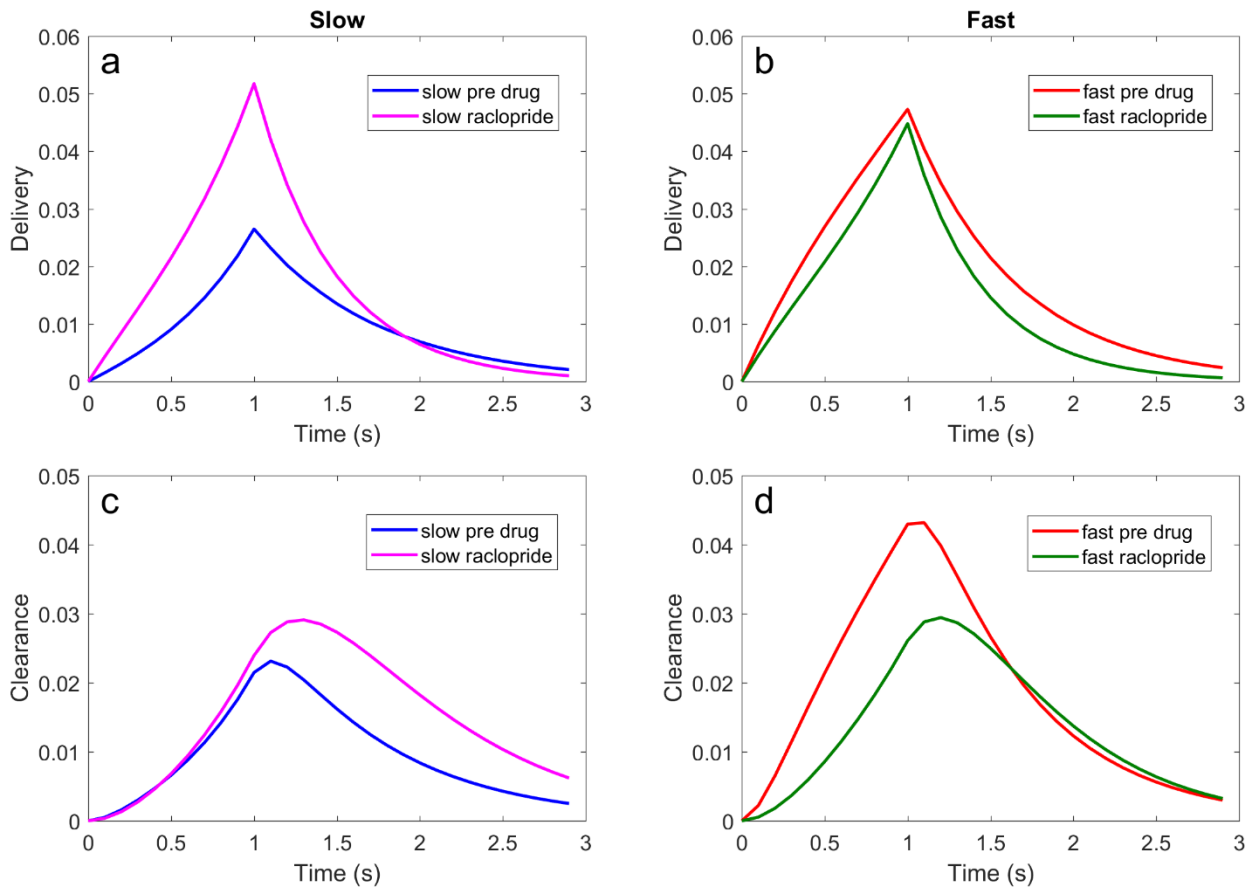
Figure 3-5

Delivery (a and b) and clearance (c and d) curves for 60-pulse, 60-Hz responses in slow (a and c) and fast (b and d) sites. Pre-raclopride curves in red and blue: post-raclopride curves in green and pink.

To examine this phenomenon one step further, we modeled responses evoked in fast and slow sites by 4 sequential 60-Hz, 60-pulse stimulus trains delivered with 2-s intervals. We reported previously that fast and slow sites respond differently such stimuli.[38] Figure 3-6a shows the delivery curves obtained for each stimulus train, while Figure 3-6b shows the corresponding clearance curves. It is immediately obvious that both the delivery and clearance curves are distinct between the fast and slow sites during the first train but not during the subsequent trains. This shows again the conversion of fast to slow behavior at initially fast sites.

Together, Figure 3-5 and Figure 3-6 reinforce the idea that the contrast between fast and slow responses at 60 Hz occur during the initial stages of the stimulus. At a stimulus frequency of 60 Hz, the fast sites produce an initial fast release component. Thereafter, the continued response closely resembles the slow response, both pre- and post-raclopride (see especially Figure 3-3c). The "conversion" from fast to slow behavior during the stimulus can be attributed to the evoked increase in extracellular DA, which presumably "turns on" autoinhibition. The conversion from fast to slow behavior is less obvious at the lower stimulus frequencies however, presumably because these lower frequencies evoke smaller increases in the extracellular DA concentration.

Figure 3-6

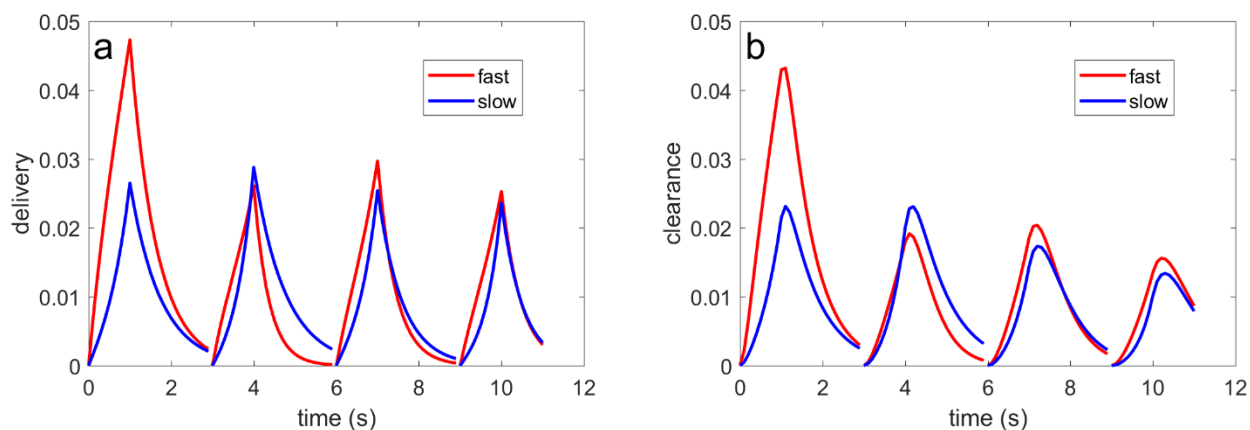We used the RD-1 model to stimulate fast and slow responses to 4 consecutive stimulus trains (60 Hz, 60 pulses, 2-s intervals). a) Delivery curves from the simulations of the fast (red) and slow (blue) responses. b) clearance curves from the simulations of the fast (red) and slow (blue) responses.

3.3.4 Analyzing the two parameter sets

As we have previously reported, the restricted diffusion models often identify two sets of adjustable parameters that produce equivalent best-fits to an evoked response.[17] This is not a mathematical mistake but rather a reflection of the fact that the model does not know a priori whether DA release and clearance are faster or slower than DA transport between compartments. Consistent with our previous work, we have chosen the parameters such that transport is slow relative to uptake ($k_U > k_T$), with k_T typically near 1 s^{-1}. This section introduces a method to confirm that the model produces only these two best-fits – local minima in the value of the sum of squared residuals (SSR). The graphical method involves plotting the SSR versus the values of the adjustable parameters (Figure 3-7).

     Figure 3-7a shows, as a representative illustration, a fast response to a 60-Hz, 60-pulse stimulus and the two, essentially identical, best-fits. Figure 3-7b shows a plot of the minimum SSR value against trial values of Rp. There are only two local minima in Figure 3-7b and the same occurs in plots of SSR against k_U and k_T. Figure 3-7c shows the delivery and clearance curves obtained with the two sets of best-fit parameters: these curves are quite different, which is why it is important to be aware that two best fits may exist. Figure 3-7d shows that, even though the delivery and clearance curves are different, the difference between them is identical: since it is this difference that determines the rate of the rise and fall of the DA concentration, this explains how the two best fits produce the same outcome.

     To date, we have only encountered simulations with at most 2 local minima: sometimes there is only one. The graphical method of Figure 3-7b confirms this. We have also noticed that a simple relationship exists between the two sets of best-fit parameters:

Equation 12

$$k_{U1} = k_{T2}$$

Equation 13

$$R_{P1} = R_{P2} * k_{T2}/k_{U2}$$

With these relationships, once one of the best-fit parameter sets is found, the other is easily calculated. Finally, simulations with only one local minimum are those with $k_U = k_T$.
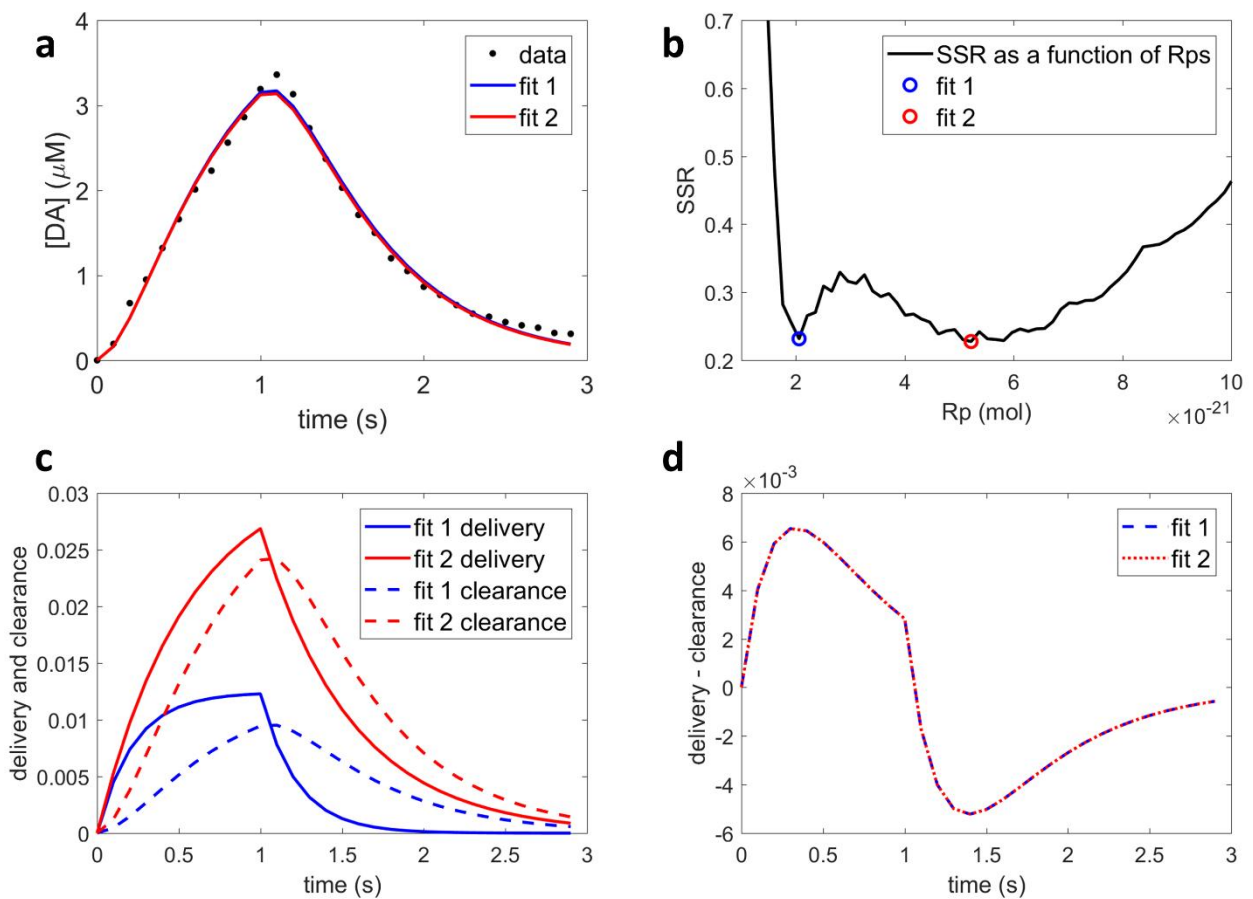

Figure 3-7

a) The 3-parameter RD model can fit the data (n=24 fast sites, 60-pulse stimulation at 60 Hz) with two sets of parameters that produce identical best fits. b) To confirm that there are only two best fits to the data, we plotted the minimum sum of squared residuals (SSR) for each tested value of R_p. c) Despite these parameters producing

identical models, the delivery and clearance curves for the two fits are different. d) The difference between each delivery and clearance curve is identical, which is why the two fits produce the same outcome.

3.4   CONCLUSIONS

This chapter developed new versions of the original RD model to produce excellent fits to a wider range of responses recorded in fast and slow sites, pre- and post-raclopride, with a variety of stimulus patterns. Versions of the RD model with 3 to 6 adjustable parameters are introduced here. The choice of model version is driven by identifying the smallest number of adjustable parameters that achieve the target of $r^2>0.99$. It is always desirable to use the smallest number of adjustable parameters. Comparing parameters across different versions of the model is not practical, but all versions have in common that the righthand side of the second of the coupled equations combines terms for DA delivery and clearance; the delivery and clearance curves are directly comparable between versions of the model. It is important to be aware of the possible existence of two local minima, which produce different delivery and clearance curves even though the modeled response is the same: a search of the parameter space confirms that at most two local minima exist.

Results obtained with the various versions of the RD model provide mathematical support for the conclusion that differences in tonic autoinhibition play a role in defining the distinct fast and slow evoked responses in the rat DS. First, at high stimulus frequency (60 Hz), administration of the D2 receptor antagonist raclopride abolishes the temporal difference between fast and slow delivery curves. Second, prolonged stimulation at 60 Hz also drives a conversion of fast to slow behaviors, which becomes most apparent during sequential 60 Hz

43

stimulus trains. Both observations, based on the characteristics of the delivery curves, indicate that autoinhibition "turns on" during the stimulus, presumably once evoked release produces sufficient extracellular DA concentrations to activate D2 autoreceptors. Consistent with this idea, the conversion of fast to slow behavior is not apparent at lower stimulus frequencies (15 and 30 Hz), which evoke less intense DA release. Thus, according to the model, the actions of raclopride on DA depend on type (fast and slow) and on the stimulus conditions.

The delivery curves were especially useful for investigating the effects of raclopride on DA release. From inspection of the parameter values alone, the identical character of the 60 Hz post-raclopride delivery dynamics in fast and slow sites (Figure 3-3c) is not in the least bit obvious. However, we also noticed that raclopride affects clearance. In the case of fast sites, our findings indicate that raclopride decreases DA clearance while not affecting release.

The observation that the fast behavior converts to slow behavior after administration of raclopride and after sufficiently intense stimulation indicates that there is no inherent difference between the DAergic terminals at fast and slow sites. Rather, the fast and slow behaviors are due to differences in the local neurochemical environment. Specifically, slow sites exhibit autoinhibitory tone, whereas fast sites do not. But, at fast sites, autoinhibition can be "turned on" by an elevation of extracellular dopamine. In summary, the work in this chapter supports the idea that the fast and slow type responses are attributable to a difference in autoinhibitory tone.

3.5   SUPPORTING INFORMATION

Table 3-1

	R_P (mol)	k_U (s^{-1})	k_T (s^{-1})	k_{R1} (s^{-1})	k_{R2} (s^{-1})	k_{U2} (s^{-1})
Figure 3-1a, 60 pulses	1.08E-21	7.4578	3.0441	-1.4444		
Figure 3-1a, 180 pulses	1.12E-21	1.7152	1.6957	-0.4886		
Figure 3-1a, 600 pulses	5.32E-20	2.1991	0.7092	0.1971	0.2891	
Figure 3-1b, 60 pulses	2.38E-21	3.0448	1.5678	-1.6970		
Figure 3-1b, 180 pulses	4.67E-21	0.9587	0.9576	-0.0391		
Figure 3-1b, 600 pulses	6.06E-21	1.0602	0.6565	0.0686		
Figure 3-1c, 60 pulses	2.50E-21	5.0038	2.7787	0.0000		
Figure 3-1c, 180 pulses	1.93E-21	4.5876	1.4757	-0.3426		
Figure 3-1c, 600 pulses	4.54E-20	1.9596	0.8034	0.1159	0.1631	
Figure 3-1c, initial fast component	4.21E-21	2.8401	0.7323	-0.0881		
Figure 3-1d, 60 pulses	3.75E-21	4.6157	1.6478	-1.0585		
Figure 3-1d, 180 pulses	3.98E-21	1.4539	1.0409	-0.0625		
Figure 3-1d, 600 pulses	3.65E-21	1.0679	0.9801	0.0542		
Figure 3-2a	4.71E-20	3.3971	1.2363	0.2334	0.3415	0.0905
Figure 3-2b	1.96E-20	3.5572	0.7414	0.2036	1.9763	0.1153
Figure 3-2c	1.76E-19	17.651	0.7183	0.1003	0.1857	0.0365
Figure 3-2c, initial fast component	4.21E-21	2.8401	0.7323	-0.0881		
Figure 3-2d	6.10E-20	18.000	0.7183	0.1939	2.1769	0.1195
Figure 3-5a/c, slow pre-drug	1.80E-21	7.5586	1.3418	-1.7607		
Figure 3-5a/c, slow raclopride	3.51E-21	1.5734	2.0776	-1.4395		
Figure 3-5b/d, fast pre-drug	6.89E-21	7.80	1.5684	-0.5293		
Figure 3-5b/d, fast raclopride	3.49E-21	2.1594	2.2394	-1.208		
Figure 3-6, slow, stimulation 1	1.81E-21	7.5586	1.3418	-1.7607		
Figure 3-6, slow, stimulation 2	1.35E-21	5.166	1.3105	-2.291		
Figure 3-6, slow, stimulation 3	1.20E-21	2.8369	1.6934	-2.0693		
Figure 3-6, slow, stimulation 4	7.00E-22	1.9971	1.957	-2.5625		
Figure 3-6, fast, stimulation 1	6.89E-21	7.80	1.5684	-0.5293		
Figure 3-6, fast, stimulation 2	2.05E-21	2.8711	2.7422	-1.0977		
Figure 3-6, fast, stimulation 3	2.37E-21	2.4268	2.3066	-1.1582		
Figure 3-6, fast, stimulation 4	2.14E-21	1.7937	2.1271	-1.125		
Figure 3-7, fit 1	2.06E-21	1.8	4.5			
Figure 3-7, fit 2	5.22E-21	4.6	1.8			

Parameters of all fits with the RD-1, RD-2, and RD-3 models. The RD-1 model uses 4 parameters, the RD-2 model uses 5 parameters, and the RD-3 model uses 6 parameters. The fits to figure 7 use the 3-parameter version of the RD-1 model.

Table 3-2

	R_P (mol)	k_U (s⁻¹)	k_T (s⁻¹)	k_R (s⁻¹)	τ	k
Figure 3-4a, slow pre-drug	1.52E-21	1.02	0.12	0.02	7.32	0.183
Figure 3-4a, slow raclopride	4.96E-21	2.46	0.08	0.04	3.91	0.141
Figure 3-4b, slow pre-drug	2.63E-21	1.44	4.58	0.046	6.60	0.695
Figure 3-4b, slow raclopride	3.62E-21	1.20	1.42	0.009	1.65	1.043
Figure 3-4c, fast pre-drug	6.60E-21	5.10	0.14	0.010	9.07	0.209
Figure 3-4c, fast raclopride	5.12E-21	2.88	0.10	0.01	7.99	0.199
Figure 3-4d, fast pre-drug	7.48E-21	14.40	0.74	-0.03	4.14	0.449
Figure 3-4d, fast raclopride	3.04E-21	3.06	1.12	-0.03	4.49	0.548

Parameters of all fits with the RD-4 model. Each case uses 6 parameters.

Figure 3-8

Fits to 15 Hz slow and fast data, pre- and post-raclopride. Parameters are reported in Table 3-2. These fits and their

parameters were used to calculate the delivery curves shown in Figure 3-4a and c.
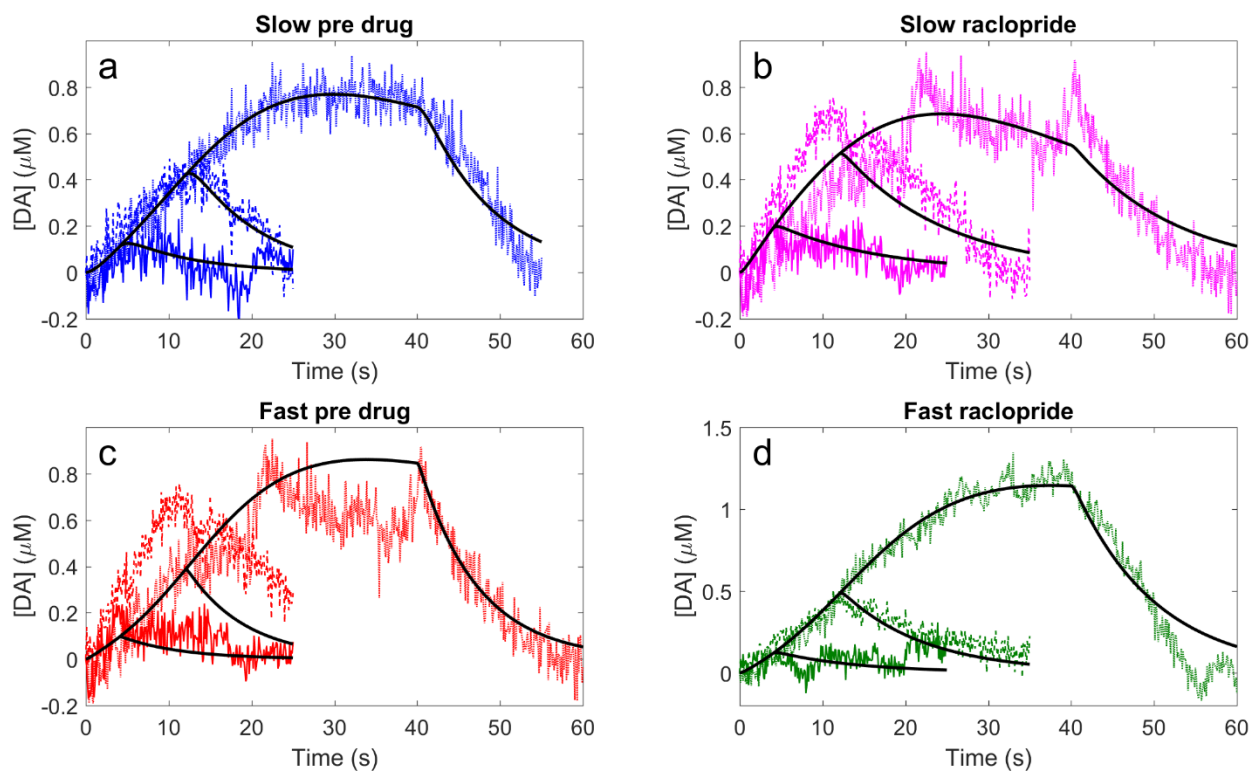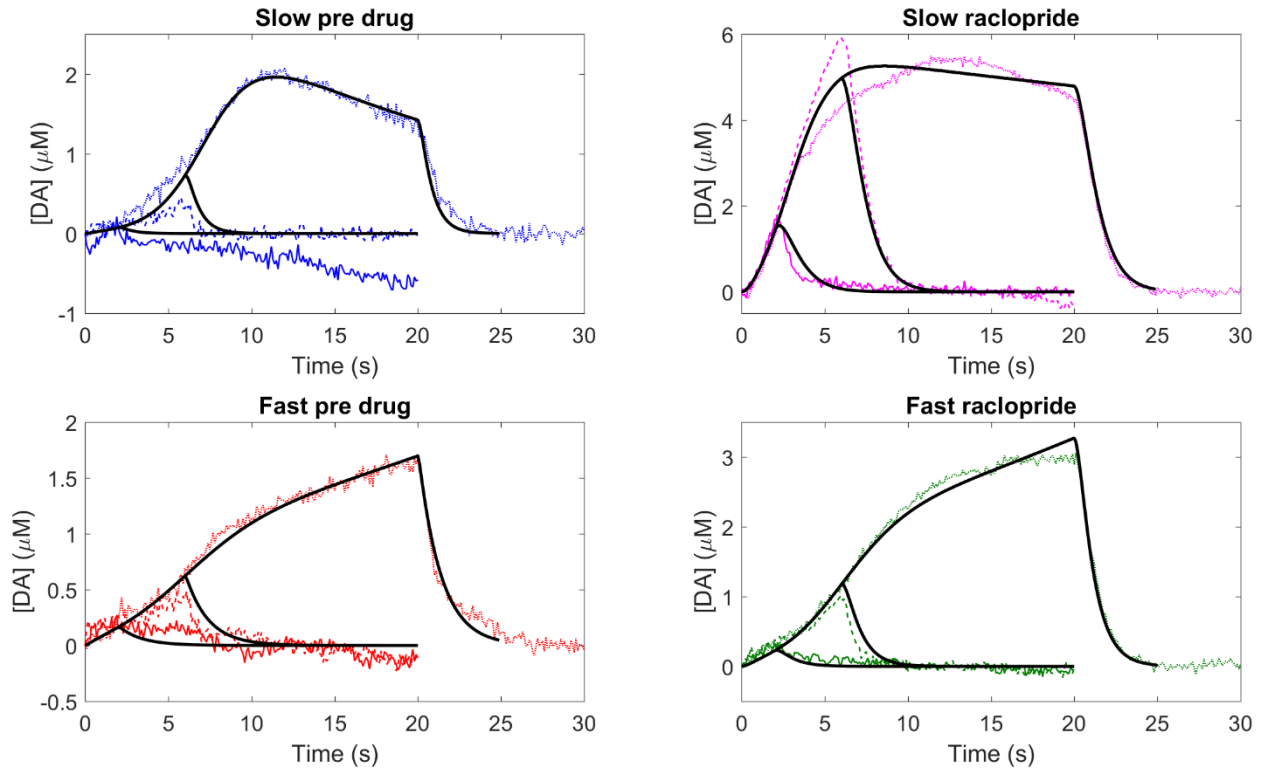
Figure 3-9

Fits to 30 Hz slow and fast data, pre- and post-raclopride. Parameters are reported in Table 3-2. These fits and their parameters were used to calculate the delivery curves shown in Figure 3-4b and d.
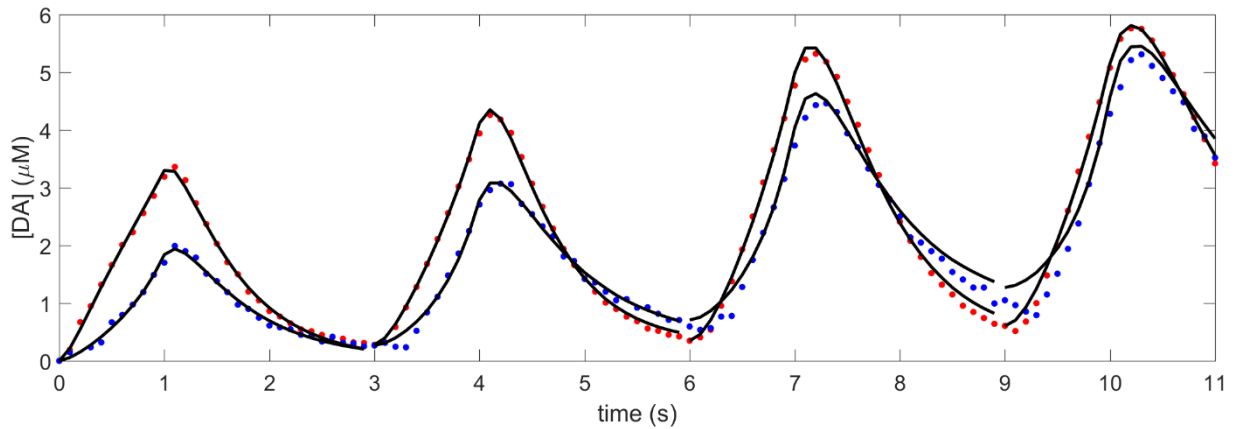
Figure 3-10

Fits to 4 repeated stimulus trains. Each stimulus was treated as an independent event for modeling purposes. Parameters for these fits are found in Table 3-1. These parameters were used to calculate the delivery and clearance curves in Figure 3-6. Slow data is in blue, fast data is in red, and the models are in black.
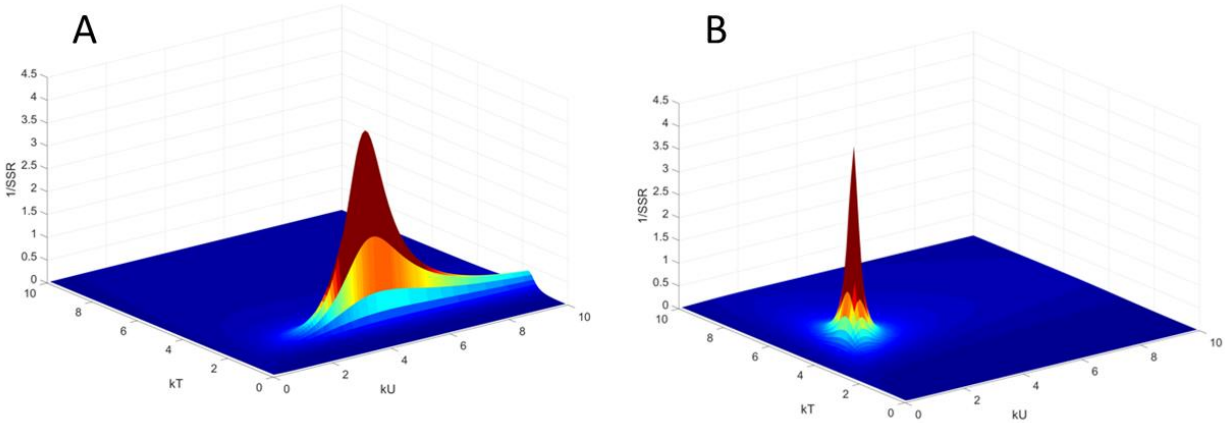
Figure 3-11

Here we show two 3D plots of the reciprocal of the SSR (for clarity of presentation) vs. k_U and k_T for two values of R_p: data are from the same fitting procedure in Figure 3-7. The chosen values of R_p for these two plots are the best-fit parameters, showing the local minima in SSR (maximum in 1/SSR). Note that most of the surface in both plots is dark blue, indicating that most regions of the parameter space that do not even come close to fitting the data. In each plot, there is one, and only one, local minimum.

4.0   EXTENDED REAL TIME METABOLIC MONITORING BY

DEXAMETHASONE-ENHANCED RAPID SAMPLING MICRODIALYSIS IN THE

INJURED RAT CORTEX

The contents of this chapter have been adapted from Robbins, E. M.; Jaquins-Gerstl, A.; Fine, D. F.; Leong, C. L.; Dixon, C. E.; Wagner, A. K.; Boutelle, M. G.; Michael, A. C. Extended (10-Day) Real-Time Monitoring by Dexamethasone-Enhanced Microdialysis in the Injured Rat Cortex. *ACS Chem. Neurosci.* **2019**. Just Accepted.

The immunohistology and fluorescence microscopy work shown in this chapter was performed by Dr. Andrea Jaquins-Gerstl.

4.1   INTRODUCION

As discussed in the introductory chapter, TBI has emerged as a major health crisis and a leading cause of death in the younger populations of many countries, including the US.[50] Severe TBI (sTBI) often involves a primary and secondary injury. The primary injury is the acute mechanical trauma, which in severe cases might require surgical intervention. Secondary injury, which likely involves several mechanisms, results in the post-traumatic expansion of the brain

lesion over the course of several days, and possibly weeks, into the vulnerable surrounding tissues, sometimes called the ischemic penumbra.[52,53,102–104] Diagnosis of secondary injury in real time is challenging.

Real-time intracerebral chemical monitoring with clinical microdialysis has been used to detect episodes of post-TBI metabolic crisis, possibly associated with the phenomenon of CSD.[1,57,105–109] Due to the progressive nature of secondary injury, sTBI patients require extended monitoring times, up to 10 days in prior studies.[4,110,111] However, during a recent study in the rat cortex, it became essentially impossible to monitor induced CSDs with conventional microdialysis by 5 days after inserting the probes.[80] Based on histochemical analyses, we attributed the difficulty to the foreign-body response of brain tissue initiated by insertion of the microdialysis probes.[11,14,45,79–81] The foreign-body response includes vasoconstriction, activation of microglia, macrophages, and astrocytes, and a loss of nearby neurons and terminals.[11,14,45,79–81] Immunostaining for the glial fibrillary acidic protein (GFAP) showed astrocyte endfeet beginning to engulf the probe track by 24 hrs after probe insertion. A glial barrier fully surrounded the probe tracks by 5 days after insertion.[11,45] Our working hypothesis is that the glial barrier impedes the detection of CSDs, possibly by inhibiting diffusion of substances to the probe from the surrounding tissues, even though basal dialysate glucose levels, possibly derived from the glial barrier, remain relatively stable.

Dexamethasone (Dex) is a glucocorticoid with potent anti-inflammatory properties.[112,113] Recent studies in the rat striatum and cortex show that perfusing microdialysis probes with low-micromolar concentrations of Dex (also called Dex retrodialysis) effectively suppresses the foreign-body response of brain tissue to the insertion of microdialysis probes.[14,79–81] Dex retrodialysis eliminates ischemia, glial activation, glial barrier formation, and neuronal losses in

the tissues surrounding the probe track. Dex also facilitates reliable monitoring of induced CSDs in the rat cortex at 1, 5, and 10 days after probe insertion. Interestingly, even though we stopped Dex perfusion 5 days after probe insertion, reliable CSD monitoring at 10 days (5 days after Dex) was preserved.[80]

The objective of the present study was to investigate whether the Dex-enhanced microdialysis is translatable to the monitoring of spontaneous CSDs in rats after controlled cortical impact (CCI), a widely studied rodent model of TBI.[114–116] CCI and probe insertion were followed by 10 days (12 days in one case) of continuous perfusion with only brief interruptions to refill the perfusion syringe. Consistent with our previously developed protocol, the perfusion fluid contained 10-µM Dex on the first day, 2-µM Dex on days 2-5, and no Dex thereafter.[14,80,81] The outlet of the probe was connected in series to a continuously recording K+ ion selective electrode (K+ ISE) and then to a rapid sampling microdialysis (rsMD) glucose analyzer.[56,104,117,118] We report herein recordings of K+ and glucose via Dex-enhanced microdialysis for 10 days (12 days in one case) following CCI and probe insertion.

4.2   METHODS

4.2.1   Reagents, solutions, and materials

All solutions were made with ultrapure water (Nanopure; Barnstead, Dubuque, IA). aCSF contained 142 mM NaCl, 1.2 mM $CaCl_2$, 2.7 mM KCl, 1.0 mM $MgCl_2$, and 2.0 mM NaH_2PO_4 (all from Sigma-Aldrich) adjusted to a pH of 7.4. Dexamethasone sodium phosphate (APP

Fresenius Kabi USA, LLC, Lake Zurich IL) was prepared in aCSF at 10 µM and 2 µM. Microdialysis perfusion fluids were filtered with 0.2 µm pore size Nalgene sterile filters (Fisher, Pittsburgh, PA; PES). GOx (100−200 units/mg) and horseradish peroxidase (≥250 units/mg) were obtained from Sigma-Aldrich. Ferrocene solution was prepared with 1.5 mM ferrocenecarboxylic acid, 1 mM EDTA, 150 mM sodium chloride and 100 mM sodium citrate and was filtered through 0.1 and 0.02 µm pore size filters.

4.2.2 Microdialysis

In-house concentric style microdialysis probes were built using hollow fiber membranes (13 kDa MWCO, Specta/Por RC, Spectrum, Ranco Dominguez, CA), 280 µm in outer diameter and 4 mm in length. Fused silica capillaries (75 µm ID, 150 µm OD, Polymicro Technologies, Phoenix, AZ) were used for the inlet and outlet lines. Probes were soaked in 70% ethanol prior to use, and then flushed with aCSF with Dex for several hours prior to implantation into the rat brain. The probe inlet was connected to a 1 mL gastight syringe driven by a microliter syringe pump (Harvard Apparatus, Holliston, MA) operating at 1.67 µL/min. The probe outlet (1.6 m long) was connected first to the K+ ISE and then to the rsMD glucose analyzer: both systems have been described in full detail in previous papers. Data were collected with LabChart (AD Instruments) and analyzed with published algorithms in MATLAB (Mathworks Inc). The K+ and glucose analyzers were calibrated at least daily. The GOx beds in the rsMD analyzer were changed at least daily, meaning that during the course of this study we used over one hundred GOx beds. Each one was calibrated with 25, 50, 125, 500, and 1000 µM glucose standard solutions. During this work, glucose was defined as non-detectable when the rsMD response was less than 3X the

baseline noise of the detector: with this criterion, we could often quantify glucose concentrations down to the single digit micromolar range. The glucose oxidase beds in the rsMD analyzer were changed every day. When dialysate glucose levels reached the rsMD detection limit the glucose sensor was calibrated to confirm its function. In addition, monitoring was continued with a new enzyme bed.

4.2.3 Surgical procedures and experimental protocol

All experiments involving animals were approved by the University of Pittsburgh's Institutional Animal Care and Use Committee. Male Sprague-Dawley rats, 250-275 g (Charles River, Raleigh, NC) were anesthetized with isoflurane (5% initially, 2.5% for maintenance and 2:1 N-$_2$O:O$_2$) and placed in a stereotaxic frame. A CCI device (Pittsburgh Precision Instruments, Inc. Pittsburgh, PA, USA) was used to create a model of mild to moderate TBI. A craniotomy was performed on the right hemisphere posterior to bregma, and the exposed dura was impacted at an average velocity of 3.9 ± 0.3 m/s, a 100 ms dwell time, to a depth of 2.2 mm. The removed bone was not replaced. The microdialysis probe was inserted 1 mm or 3 mm anterior to the craniotomy at a 51° angle so that the entire dialysis membrane was placed into the cortex. During data acquisition, we observed no systematic effect of the 1- or 3-mm probe location, so data from the two locations were pooled. The probe was secured with bone screws and dental cement, and the incision was closed with sterile sutures. Rats were housed in a Rarturn Microdialysis Bowl (MD-1404, BASI, West Lafayette, IN). The probes were continuously perfused with 10 µM Dex for the first 24 hr, followed by 2 µM Dex for days 2-5, and aCSF (no Dex) for the remainder of the experiment. Microdialysis monitoring was performed in a total of 10 rats. In 8 rats,

microdialysis continued for 10 days. In one rat, at the end of 10 days, both the K+ and glucose levels were stable and at normal baseline levels, so monitoring was extended to 12 days. The first rat in this study broke the connections to the microdialysis probe 18 hrs after surgery: up to that point, the experiment had been progressing normally, so the data are included in this report. Subsequent rats were fitted with an Elizabethan collar (MF-53721, BASi, West Lafayette, IN). Three CCI-naïve, control rats underwent the same 10-day Dex-enhanced microdialysis protocol as just described: we ran 31 CCI-naïve control rats in our prior study [80].

4.2.4 Immunohistochemistry and fluorescence microscopy

As mentioned above, the immunochemistry and fluorescence microscopy data reported in this chapter were collected by Dr. Andrea Jaquins-Gerstl. Rats were anesthetized with isoflurane (2.5% by volume O_2) and transcardially perfused with 200 mL 0.01 M of pH 4 phosphate-buffered saline (PBS), 160 mL of 4% paraformaldehyde, and 50 mL of PBS containing 100-nm fluorescent beads (Molecular Probes, 1:1000 dilution in PBS). The brain and probe were removed and further fixed in 4% paraformaldehyde for 24 h at 4 °C. The tissue containing the probe track was cut to 35 μm thin horizontal sections (3 slices per antibody per animal). Free floating sections were rinsed in PBS (3 x 10 min), blocked (3% goat serum in PBS containing 0.1% Triton X-100) for 1 h at room temperature, and immunostained for 24 hours at 4 °C. Primary antibodies were anti-glial fibrillary acidic protein (GFAP; 1:100, DAKO Agilent Technologies), NeuN (1:100, Chemicon, Temecula, CA), and ED-1 (1:100, AbD Serotec, Raleigh, NC). Sections were washed with PBS (10 min) and incubated in 3% goat serum, 0.1% Triton X-100, and 1:500 goat anti-rabbit Alexa 568 (Invitrogen, Carlsbad CA) for 2 h at room

temperature. Sections were rinsed with PBS (10 min) and cover-slipped with Fluoromount-G (Southern Biotech, Birmingham AL). Sections were imaged with a FluoView 1000 (Olympus, Inc., Tokyo, Japan) at 20× magnification.

4.2.5   MALDI-MS

Samples of dialysate were collected offline and frozen at -20 °C until use. For matrix-assisted laser desorption/ionization (MALDI) mass spectrometry (MS) analysis, samples were mixed with matrix in a 5:1 matrix to sample ratio. The matrix solution was a 10 mg/mL solution of sinapinic acid (Sigma-Aldrich) in 50:50 water and acetonitrile with 1% difluoroacetic acid. Samples were plated with the dry drop method and run on a Bruker Daltonics UltrafleXtreme MALDI TOF-TOF instrument equipped with a Nd:YAG laser (Bruker, Billerica, MA). Samples were run in reflectron positive ion mode with 10 consecutive laser shots.

4.3   RESULTS AND DISCUSSION

4.3.1   Summary of observations

We recorded K^+ and glucose in dialysates from 10 rats for 10-12 days following CCI and microdialysis probe insertion. Recordings from n=8 rats exhibited 185 spontaneous CSDs, hallmarked by a transient rise and fall in dialysate K^+, typically over the course of 5-7 min. All CSDs were spontaneous, meaning none of them were induced by the pin-prick method of our previous work.[80] Of the CSDs observed while we were also monitoring glucose (n=126), some

were accompanied by negative glucose transients (n=89), no obvious change in glucose (n=25), or transient increases in glucose (n=12). In one rat, CSDs were observed as late as 12 days after CCI. Some rats (n=2) exhibited no CSDs, which seems to be consistent with clinical reports that CSDs are detected in some but not all TBI patients who undergo neuromonitoring. We have not observed spontaneous CSDs in any CCI-naïve control rats (n=3) in this work or in prior studies (n=31).[80] Table 4-1 provides a summary of observations from each subject.

We also observed a second post-CCI phenomenon consisting of a slow, progressive decline of dialysate glucose from basal to, eventually, concentrations below the detection limit of the rsMD glucose analyzer. Once this occurred, glucose concentrations did not return to detectable levels. The onset of the glucose decline was highly variable between rats: in one case, it occurred on day 12 after CCI. In some cases, after glucose declined, the K^+ level steadily increased, indicating a loss of K^+ homeostasis. Occasional CSDs were observed after glucose declined. We have not observed this glucose decline in any CCI-naïve control rats. Figure 4-1 through Figure 4-5, below, report K^+ in purple and glucose in red.

Table 4-1

	Probe location	# of CSDs observed	Glucose ND (hr)	CSDs per hr observation	Notes
Rat 1	1 mm	58	N/A	3.149	Rat broke the probe about 18 hours after implantation – until then, CSDs nearly constant
Rat 2	1 mm	12	81	0.067	
Rat 3	1 mm	11	N/A	0.070	Large fluctuations in glucose concentrations over time
Rat 4	1 mm	0	29	0	
Rat 5	1 mm	0	56	0	

Rat 6	3 mm	19	284	0.140	CSDs continued until day 12, stopping a few hours before glucose reached ND level
Rat 7	3 mm	19	164	0.336	
Rat 8	3 mm	7	43	0.064	Abnormal movements, presumably seizures, correlated with K^+ fluctuations after glucose reached ND level
Rat 9	3 mm	20	37	0.183	
Rat 10	1 mm	39	106	0.359	

A summary of observations from each rat in this study. Probe location is the distance from the edge of the CCI lesion to the probe track: we noticed no systematic effect of probe location during this study. The column titled Glucose ND (hr) gives the time, in hours from the CCI, when glucose declined to below the detection limit.

4.3.2 Individual observations: spontaneous spreading depolarizations

Figure 4-1 reports representative examples of the 185 spontaneous CSDs observed during this study. Figure 4-1 clearly shows the CSD profile from the recording of K+, wherein the K+ concentration transiently rises and falls over the course of 5-7 minutes. Figure 4-1A shows a single, isolated CSD event accompanied by a negative glucose transient. The fall in glucose, which is coincident to the rise in K+, reflects the energy demand associated with tissue repolarization after the CSD. Figure 4-1B shows two CSDs about 10 min apart, which qualifies them as a CSD cluster.[51,119] CSD clusters are of special interest because, as in this example, the second CSD might force a second negative glucose transient superimposed on the first one. Another noteworthy difference between Figure 4-1A and B is the magnitude of the glucose data: in Figure 4-1A, the glucose baseline is near 20 µM and is forced to non-detectable levels by the CSD whereas in Figure 4-1B the glucose baseline is near 600 µM and only partially declines

after the CSDs. The origin of this wide variation in the glucose baseline is discussed further, below. Figure 4-1C shows a CSD accompanied by a rise in glucose, possibly indicating a change of blood flow.

Figure 4-1 illustrates the potential value of microdialysis in the diagnosis of CSD-associated secondary injury. The K+ signal identifies CSDs, as does electrocorticography (ECoG), a widely used neuromonitoring tool.[53,80,103,104,106,118] However, ECoG and related recording techniques do not provide real time chemical information that might prove useful in identifying which CSDs trigger glucose declines (Figure 4-1A and B) and which do not (Figure 4-1C). This is potentially important information because the glucose decline, a form of metabolic crisis that might deprive cells of the energy they need for basic survival, has been identified as a potential mechanism for secondary injury.[107,120–122]

Figure 4-2 shows representative recordings of dialysate K+ and glucose over hours-long time blocks, from separate rats, at various times after probe insertion (spontaneous CSDs are marked with arrows). The data in Figure 4-2A through E were obtained on day 1 of the recording session. Figure 4-2A and B show cases where multiple CSDs and CSD clusters were accompanied by negative glucose transients. Figure 4-2A also shows a likely seizure (asterisk). In the case of Figure 4-2C, no CSDs were observed and the K+ and glucose concentrations were consistent with the normal basal range (370±40 µM, mean±SEM) from CCI-naïve animals [80]. The data in Figure 4-2D and E exhibit CSDs isolated in time and not part of a cluster. In Figure 4-2D the CSDs are accompanied either by an increase or no change in the glucose level. In Figure 4-2E, the CSDs are accompanied by negative glucose transients. The data in Figure 4-2F and G were collected 10-12 days after probe insertion. Figure 4-2F shows an isolated CSD, confirming the potential of Dex-enhanced microdialysis to record CSDs 12 days after injury: in

58

this case, due to the low glucose baseline (explained below) it is unclear whether this CSD caused a glucose transient. The data in Figure 4-2G are from a CCI-naïve, control rat: we have observed no spontaneous CSDs in any CCI-naïve animals (this study, n=3: Varner et al., n=31).[80]
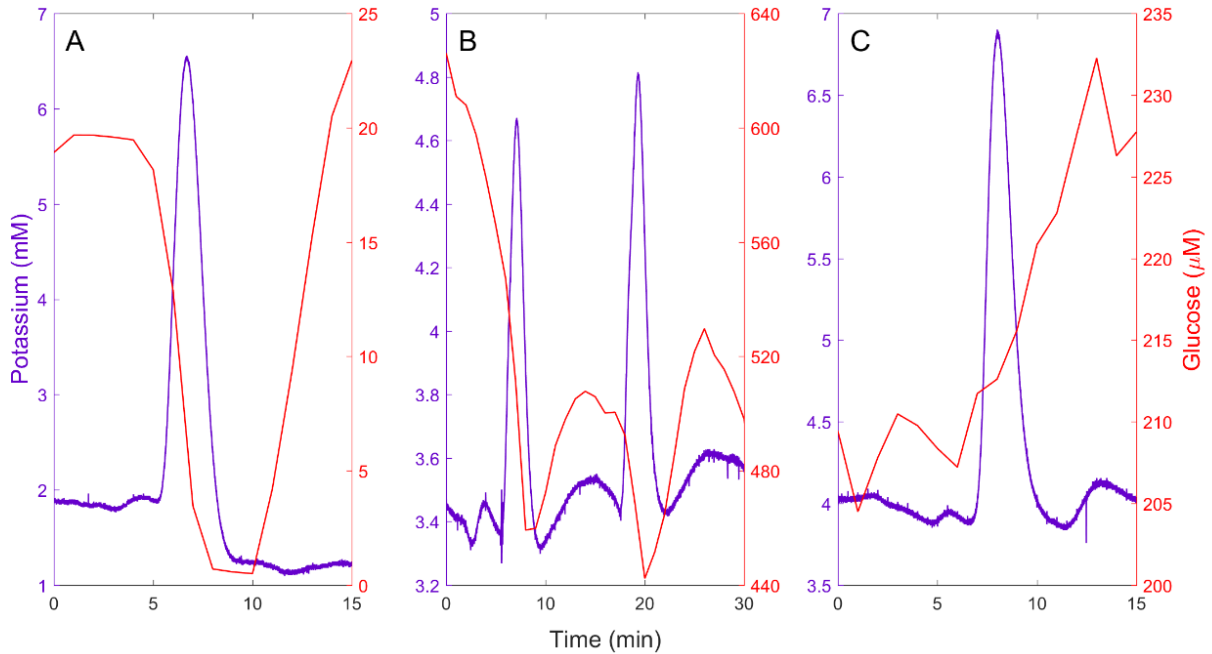

Figure 4-1

A) An isolated spontaneous CSD accompanied by a negative glucose transient. B) A cluster of two closely spaced spontaneous CSDs: the second CSD triggers a negative glucose transient before the complete recovery of the prior negative glucose transient. C) A spontaneous CSD accompanied by an increase in glucose, possibly indicating a change in blood flow.
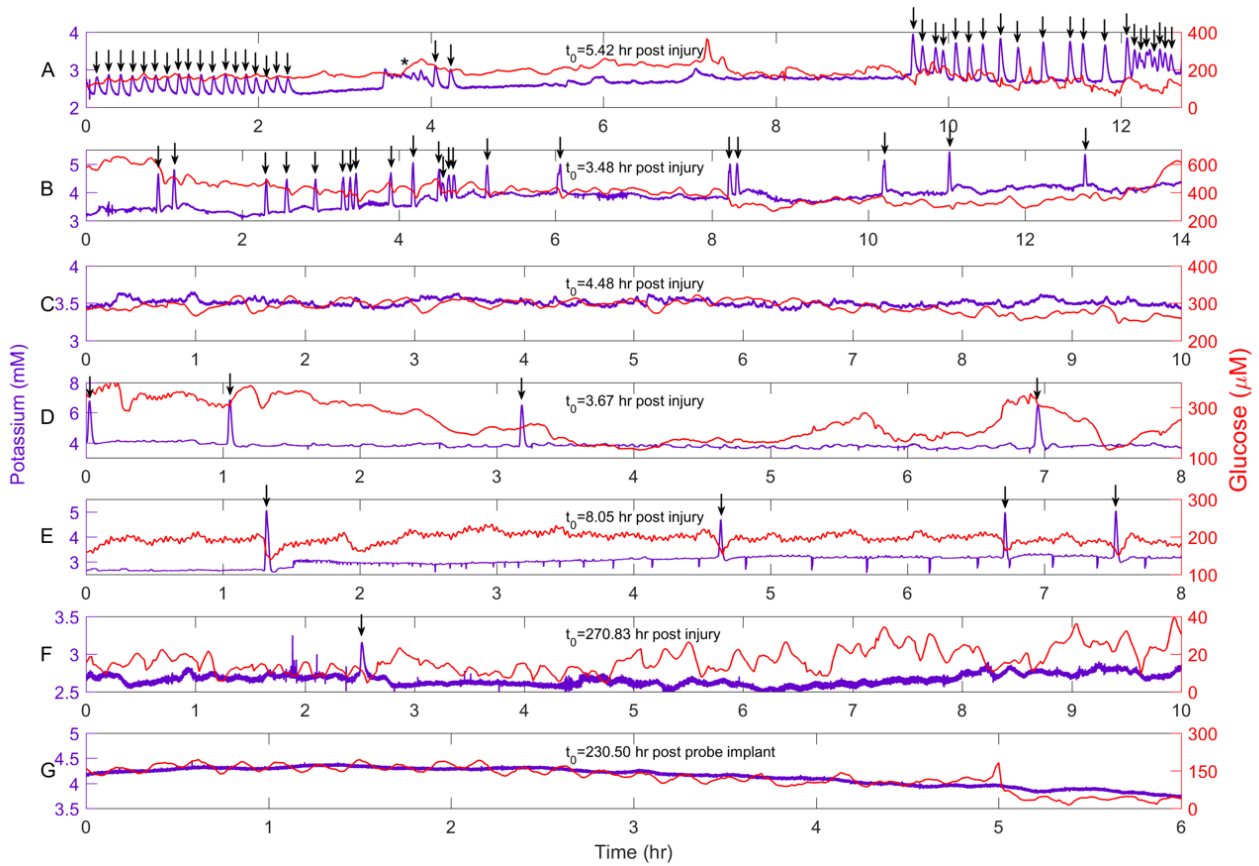
Figure 4-2

Representative recordings of dialysate K+ (purple) and glucose (red) from seven different rats. The data in Panels A-E were collected within the first 24 hr after CCI and probe insertion. A and B) Rats 1 and 10 exhibited numerous CSDs and CSD clusters, some of which were accompanied by negative glucose transients. C) Rat 4 exhibited no CSDs. D and E) Rats 2 and 6 exhibited isolated CSDs. F) Rat 6 exhibited a spontaneous CSD 12 days after CCI and probe insertion. G) CCI-naïve control rats do not exhibit spontaneous CSDs. Arrows mark spontaneous CSDs.

4.3.3 Individual observations: the progressive glucose decline

All but two rats in the CCI group (one of which broke his probe) exhibited a progressive decline in dialysate glucose concentration (Figure 4-3). The glucose concentration declined from the normal basal range over a period of several hours, eventually falling below the detection limit of

60

the rsMD glucose analyzer. In Figure 4-3, the glucose level at the start of the time block is near 10% of the normal basal range (370 ± 40 µM),[80] so this recording shows the final stage of the decline to the nondetectable (ND) level (in the figures, "Glucose ND" means nondetectable glucose). Furthermore, in this case, the K+ trace is featureless, exhibiting no CSDs and a relatively stable signal (see below for examples of the other K+ responses). With Dex-enhanced microdialysis, we have observed no such glucose declines in any CCI-naïve control animals (n total = 34).

Four of the eight rats exhibiting the progressive glucose decline also exhibited an accompanying rise in dialysate K+, indicating a loss of K+ homeostasis (Figure 4-4). In one case (Figure 4-4A), the K+ concentration rose suddenly when glucose finally reached the detection limit. In other cases (Figure 4-4B and C), K+ rose progressively as the glucose concentration declined. An isolated spontaneous CSD that occurred while glucose was low, but still detectable, forced glucose transiently to the ND level (Figure 4-4C, see Figure 4-5A for another example). Typically, the glucose concentration hovered for several hours at a few percent of the normal basal range before eventually falling below the detection limit (Figure 4-4A and C). Two rats exhibited abnormally large spikes of glucose, into the hundreds-of-micromolar range, just prior to glucose reaching the detection limit (Figure 4-4A); the origin of these rare spikes is unknown.

Isolated CSDs occurred during and after the progressive glucose decline (Figure 4-4C and Figure 4-5A and B). These CSDs occurred regardless of whether the K+ concentration was relatively stable (Figure 4-5A) or exhibited a progressive rise (Figure 4-5B) once glucose reached the ND level. In one case, several days after glucose reached the ND level, K+ exhibited numerous small-amplitude fluctuations superimposed on an unusually high background (Figure 4-5C). These fluctuations lasted for several hours, during which the animal exhibit repeated

abnormal movements of the head, trunk, and forelimbs. We assume the animal was having seizures.
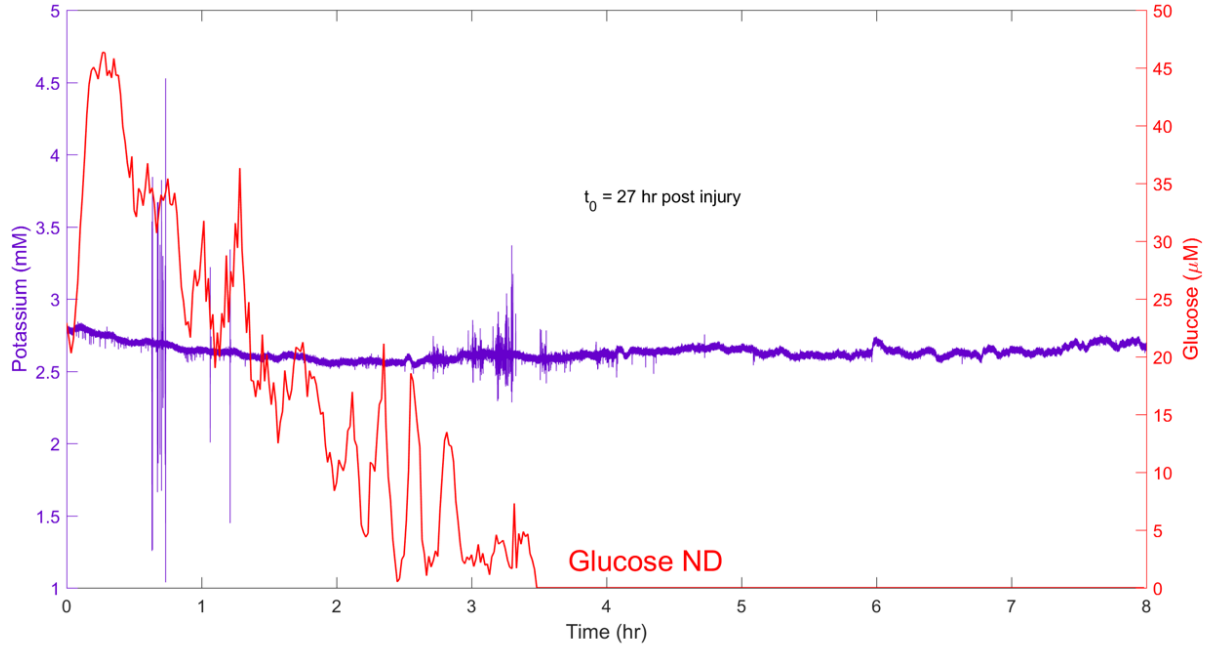

Figure 4-3

A representative example of the post-CCI progressive glucose decline from Rat 4. "Glucose ND" means non-detectable glucose below the detection limit of the rsMD glucose analyzer. In this case, CSDs were not observed and the dialysate K+ concentration remained relatively stable.
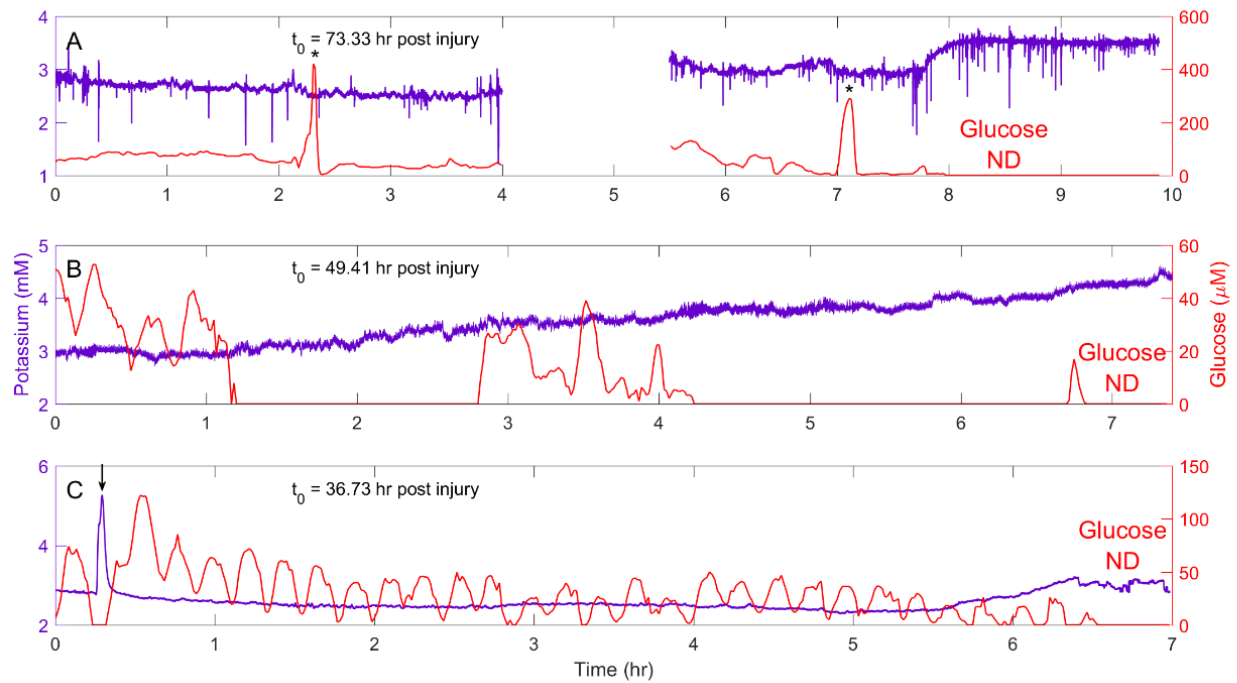
Figure 4-4

Examples of the progressive glucose decline accompanied by a loss of K+ homeostasis. A) Rat 2 exhibited rare but huge glucose spikes during the progressive glucose declines (asterisks). When glucose eventually fell below the detectable level (at 7.8 hr), K+ exhibited a sudden rise. The gap in the data occurred because it was necessary to refill the perfusion syringe. B) Rat 5 exhibited a progressive glucose decline accompanied by a progressive rise of K+. C) Rat 8 exhibited a progressive rise in K+ just as glucose reaches the ND level: a spontaneous CSD (arrow) forces glucose to fall from its already low level to ND.
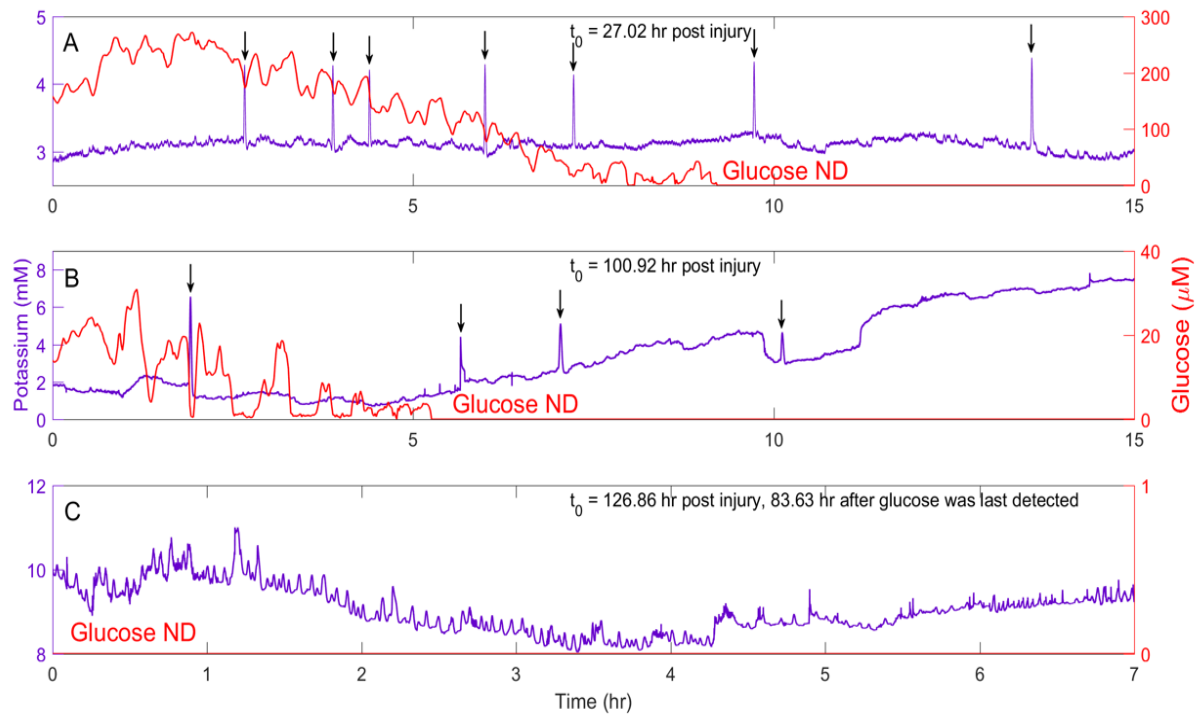
Figure 4-5

Spontaneous CSDs before and after glucose reaches the ND level. A) Rat 9 exhibited CSDs when K+ was relatively stable over time. B) Rat 10 had CSDs as K+ exhibits a progressive rise. C) Rat 8 had numerous small-amplitude K+ fluctuations superimposed on a relatively high K+ background. The animal exhibited unusual movements during this time block. We assume the animal was having seizures. Arrows indicate spontaneous CSDs.

4.3.4 Immunohistochemistry

At 10 or 12 days after CCI and probe insertion, the animals were re-anesthetized, the probes were carefully extracted, and brain tissues were fixed, sliced (30-µm sections) in the plane perpendicular to the microdialysis probe, and processed for immunohistochemistry. Figure 4-6 shows a representative DIC image of a CCI lesion with an adjacent probe track: a separate panel shows the probe track at higher magnification. The CCI lesion appears as a hole surrounded by a

darkened, presumably necrotic border. Figure 4-7A shows fluorescence images of two probe tracks. The markers in this image are for blood vessels (nanobeads), macrophages (ED-1), astrocytes (GFAP), and neurons (NeuN). The left and right columns show probe tracks placed 1 and 3 mm, respectively, from the CCI lesion: as mentioned in the Methods section of this chapter, these placements had no apparent systematic impact on the outcome of any of the measurements reported herein. Essentially, these probe tracks are similar in appearance to those of Dex-perfused probes in CCI-naïve animals reported in our previous studies.[13,14,45,80] Quantitative analysis of blood vessel and GFAP images of probe tracks from CCI and CCI-naïve animals found no statistically significant difference (Figure 4-7B). Specifically, the images show intact blood vessels, minimal glial activation, and no evidence of a glial barrier. These findings confirm that Dex retrodialysis is an effective means of mitigating the foreign-body response to the insertion of microdialysis probes into the injured rat cortex. We emphasize again that these images show tissues 10 days after CCI and probe insertion but 5 days after halting Dex retrodialysis.

Figure 4-8 shows images of the border of the CCI lesion (see Figure 4-6). These images show that the border is a zone of ischemic tissue that lacks signs of blood flow (nanobeads) and contains activated macrophages and glia and few if any surviving neurons. The images do not show any clear signs that Dex delivered via the microdialysis probe had any mitigating effect on the CCI lesion, such as a local reduction in ED-1 or GFAP or increase in blood flow or NeuN. Thus, Dex appears to have acted only to mitigate the foreign-body response of the brain tissue to the probe insertion, which is consistent with our previous observation of Dex diffusing no more than about 100 μm from microdialysis probes.[14] This is important in the context of future efforts

to translate Dex-enhanced microdialysis to the clinical setting, where the goal will be to monitor, rather than treat, the injured brain.
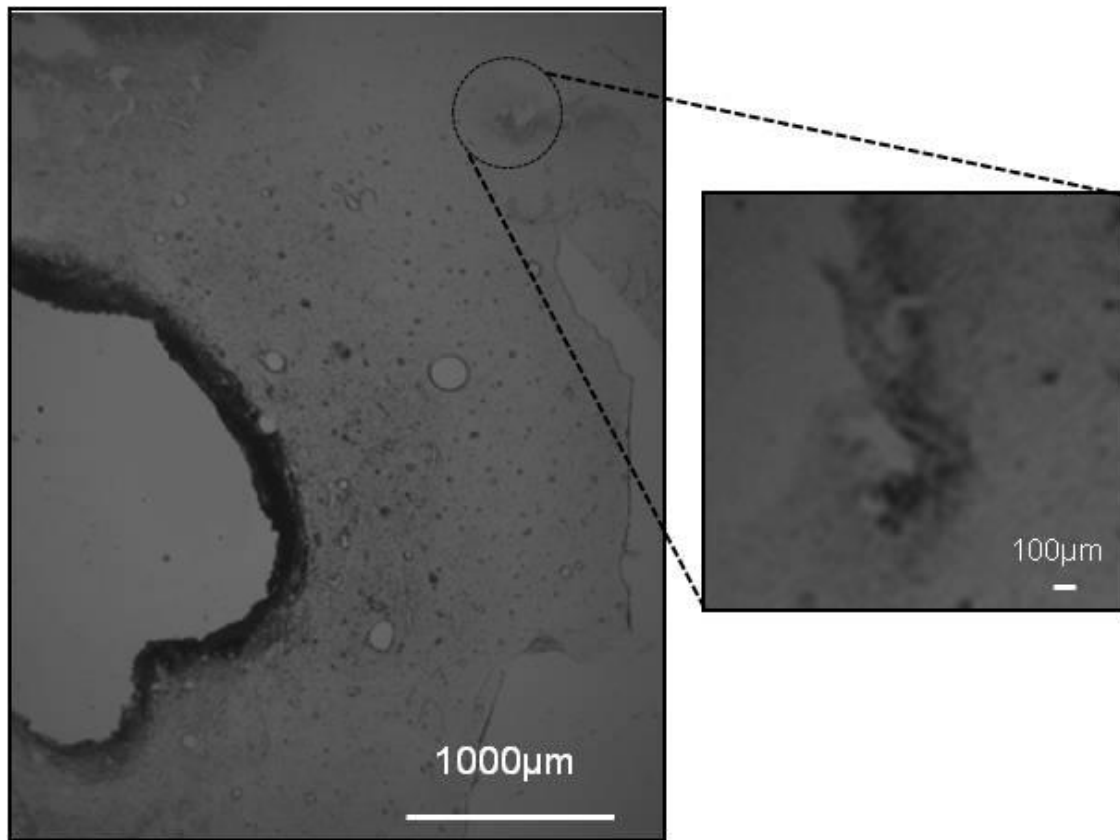
Figure 4-6

DIC image of a thin section of brain tissue passing through the CCI lesion and the track of a microdialysis probe: the image on the right shows the probe track at higher magnification.
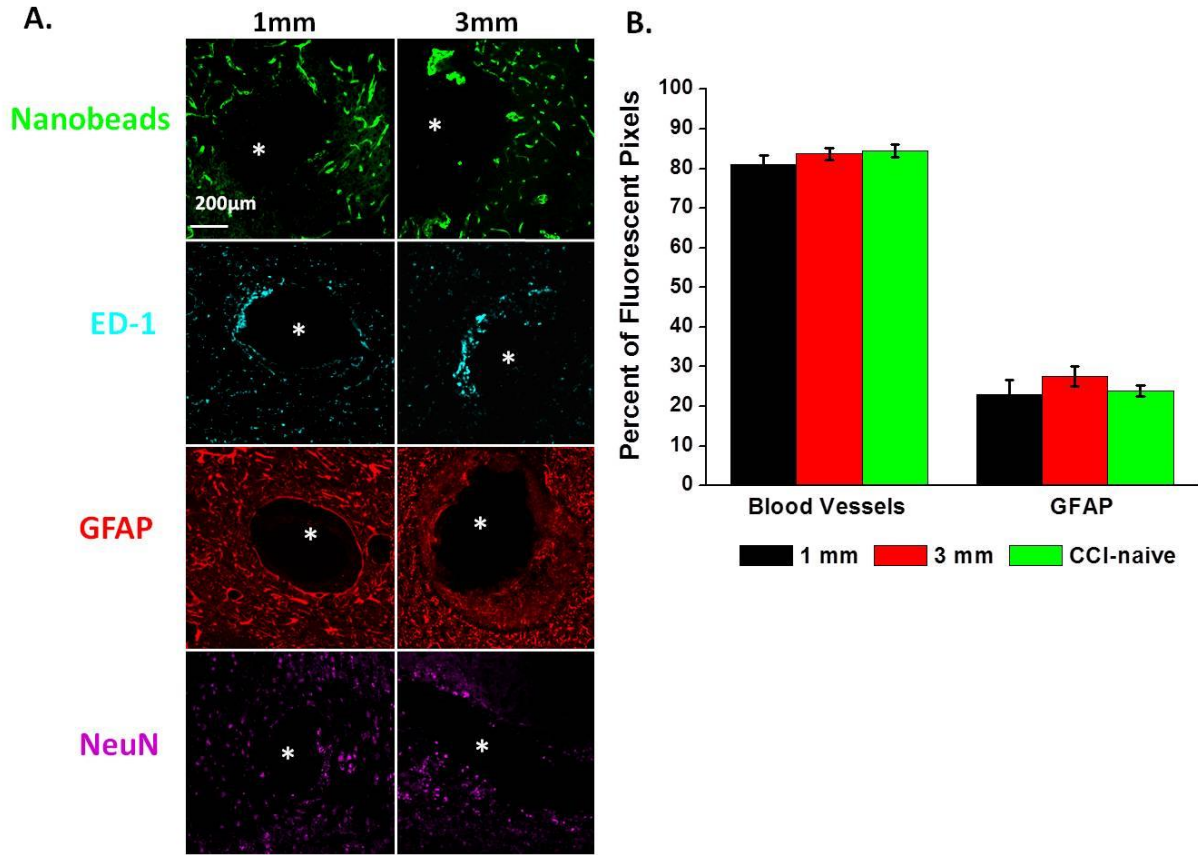
Figure 4-7

A) Images of two probe tracks from the CCI group showing markers for blood vessels (nanobeads), macrophages (ED-1), astrocytes (GFAP), and neurons (NeuN). The left and right columns show probe tracks located 1 and 3 mm, respectively, from the CCI lesion. B) Quantitative analysis of blood vessel and GFAP images of probe tracks from CCI and CCI-naïve control animals: results are reported as percent of fluorescent pixels (mean±SEM, no significant differences between images from CCI and CCI-naïve animals, t-test).
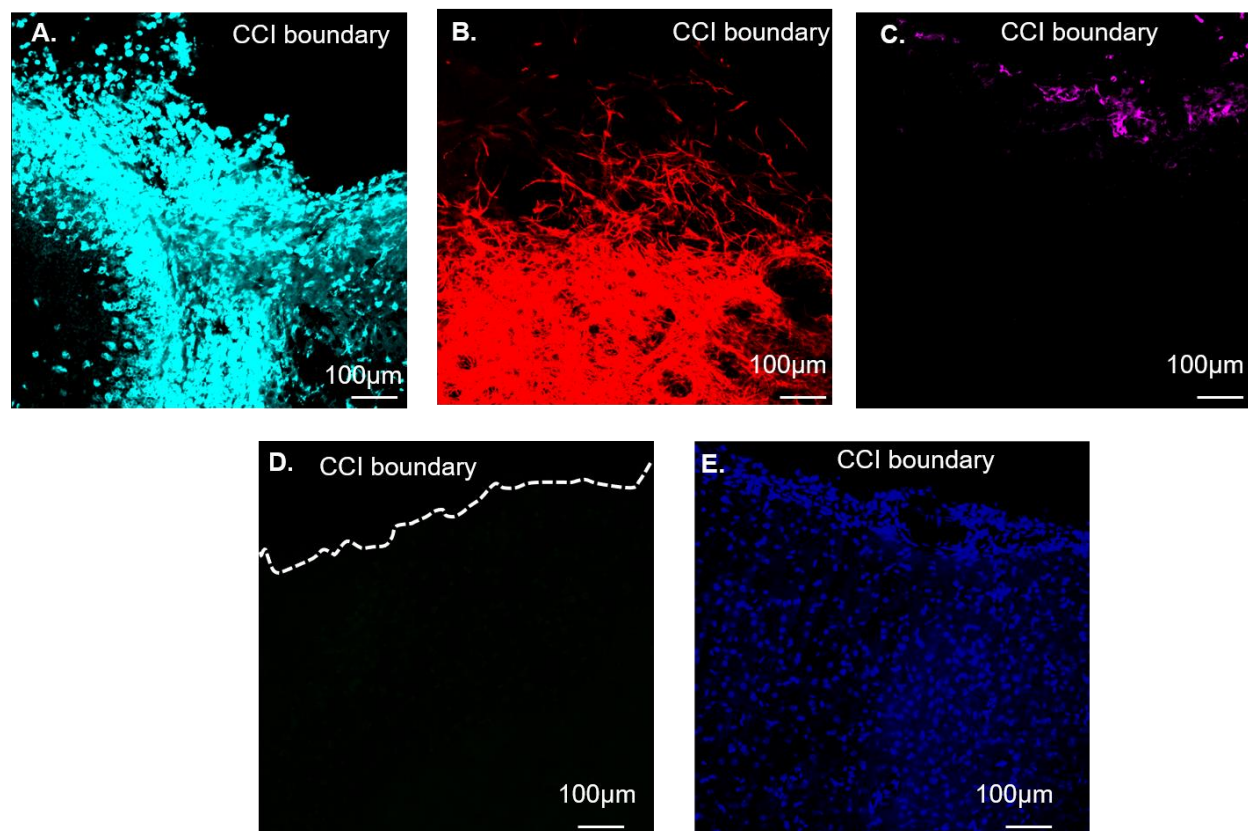
Figure 4-8

Fluorescence microscopy of the boundary region of the CCI lesion. The markers show A) macrophages (ED-1), B) astrocytes (GFAP), C) neurons (NeuN), D) blood vessels (nanobeads), and E) nuclei (DAPI): a white dotted line has been added to D) to indicate the location of the tissue boarder. These images show that the boarder of the CCI lesion is an ischemic zone with activated glia and a loss of neurons.

4.3.5 Dialysate analysis by MALDI-MS

We wished to confirm that the progressive decline in dialysate glucose level (Figure 4-3 through Figure 4-5) is not due to an unexpected loss in permeability of the microdialysis membrane, due perhaps to increased inflammation in the injured tissue. To this end, we collected dialysate samples for offline analysis by MALDI-MS. Samples were collected from control rats (no CCI)

on days 1 and 10 after probe insertion and from CCI-injured rats before and after the progressive glucose decline: Figure 4-9 reports representative mass spectra from each of the four experimental conditions. The spectra all show that the dialysate contains brain-derived species in the m/z range of 300-1500, whereas the molecular weight of glucose is 180 Da. These spectra confirm that the microdialysis membranes remain permeable to a range of species in both control and CCI-treated rats. Consistent with the histology of the probe tracks, these data further verify the anti-inflammatory efficacy of Dex-retrodialysis in both control and CCI-treated cortex.
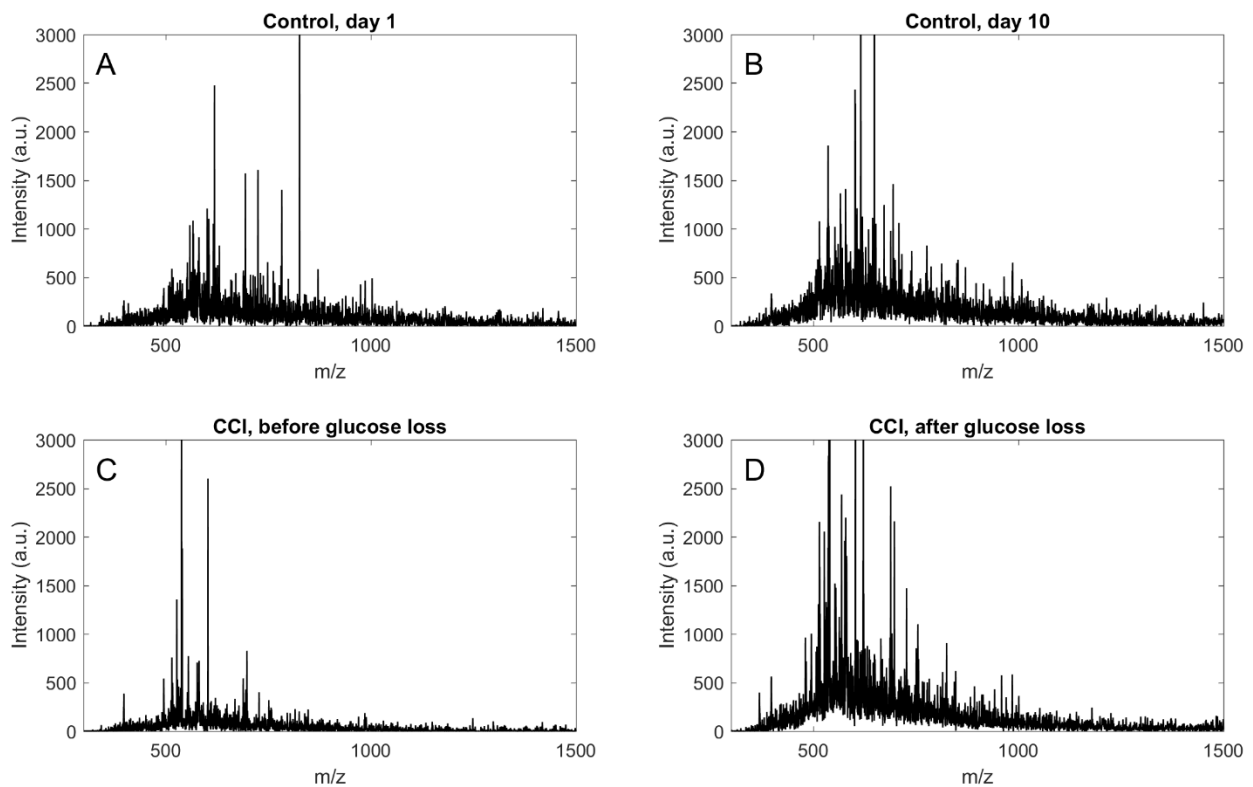

Figure 4-9

MALDI-MS spectra of dialysate samples collected from control rats (no CCI) on A) day 1 and B) 10 after probe insertion and from CCI rats C) before and D) after the progressive decline in dialysate glucose levels.

4.4   CONCLUSIONS

The findings of this study confirm the successful translation of Dex-enhanced microdialysis to the CCI rodent model of TBI. Specifically, Dex retrodialysis effectively suppressed the foreign-body response of brain tissue to probe insertion adjacent to a CCI lesion, thereby facilitating the pericontusional monitoring of K+ and glucose during the course of 10-12 days post-CCI. Perfusion of the probe was continuous over this time interval. K+ and glucose levels were monitored for 10-15 hr time blocks but not constantly.

We found a high degree of animal-to-animal variability in the outcome of chemical monitoring after CCI. Individual animals varied widely in the number and frequency of CSDs and the onset and duration of progressive glucose decline. We tentatively attribute this to the varied extent of the injury induced by CCI. Whereas the CCI per se was tightly controlled, the resultant injury was not. In some animals, the injury was confined to the cortex but in others it penetrated into subcortical structures, with variability in the overall volume of ablated tissue. The probes were positioned at 1- and 3-mm from the edge of the impact site (Table 4-1) in anticipation of observing some sign that secondary injury spreads over time into the penumbra, but this did not happen. Two of the animals with probes at 3 mm exhibited the latest onset of progressive glucose decline, but two others exhibited onsets like those in animals with probes at the 1 mm location (Table 4-1). Given the variability in the extent of injury, it is likely that the number of animals presented in this chapter was too small to identify differences between the 1- and 3-mm location.

Despite the animal-to-animal variability, this study yielded several consistent observations. Most rats (8 of 10) exhibited spontaneous CSDs, either isolated or in clusters. It is

not altogether surprising that no CSDs were observed in two subjects. First, clinical neuromonitoring detects CSDs in only about 60% of TBI patients, suggesting that CSDs may not be a universal symptom of TBI.[54] Of course, the incidence of CSDs is likely affected by the severity of TBI, which was highly variable in this study. Second, it is important to acknowledge that the microdialysis probe only monitors at a single tissue location, so it is possible that CSDs occurred at remote locations. Numerous spontaneous CSDs were accompanied by negative glucose transients, which have become a subject of intense interest as a potential mechanism of CSD-associated secondary injury.[109,111,123–125] However, some CSDs appeared to have no effect on glucose or were accompanied by an increase in glucose possibly caused by a change in blood flow.[107,122] Discriminating between CSDs that do and do not induce metabolic crisis could be of clinical importance. A second consistent observation, but apparently independent of CSDs, was the progressive decline in dialysate glucose output. This occurred in all CCI rats except two, one of which prematurely broke its probe (Table 4-1). The decline started at various times after the CCI, 12 days after CCI in one case, and typically lasted for several hours until glucose concentrations eventually became too low to detect. Once glucose reached the nondetectable level, it did not return to detectable levels at a later time. Spontaneous CSDs occurred before, during, and after the glucose decline. In one animal, the glucose decline occurred in the absence of CSDs. In approximately half the cases, the decline in glucose was accompanied by a rise in K+, suggesting a failure of K+ homeostasis. Although additional data would be desirable to confirm this, CSDs and the progressive declines in glucose appeared to be independent consequences of CCI.

Vespa et al. also observed dramatic declines in glucose by microdialysis in TBI patients.[4,126] In contrast to our observations, in which glucose fell to non-detectable levels in 8 of

10 rats, Vespa et al. reported this in 6 of their 30 patients.[4,126] Moreover, Vespa et al. reported that the decline was associated with terminal herniation, whereas our CCI protocol induced no terminal events. Additionally, it is important to mention that Vespa et al. intentionally avoided pericontusional probe locations, whereas we placed the probes adjacent to the CCI lesions. These findings, and their contrast with those of Vespa, might suggest that a progressive glucose decline may be a common but non-terminal event in ischemic penumbral zones and might signal a local metabolic crisis involved in secondary injury and expansion of the CCI lesion.

We wish to be duly cautious in interpreting the progressive glucose decline. We must consider the possibility that it is related to the permeability of the microdialysis membrane. Whereas data from control animals shows that microdialysis probes continue to recover glucose from the brain for up to 10 days, it is possible that CCI triggers a more intense inflammatory response to probe insertion, resulting a loss of glucose recovery. Several observations speak against this possibility. First, even in animals exhibiting the glucose decline, examination of the probe tracks did not show the presence of a glial barrier, absence of blood flow, or profound losses of neurons: these observations indicate the anti-inflammatory efficacy of Dex in the presence of CCI. Second, even after the progressive decline in glucose we continued to detect K+, including increases in K+ levels, CSDs, and seizures: this confirms that the probes remain permeable to K+. Third, MALDI-MS did not indicate systematic differences in composition of the dialysate under four conditions (without CCI on days 1 and 10, with CCI before and after the glucose decline of glucose). The MALDI data indicate that the probes remain permeable to a range of brain-derived species, including species with higher molecular weight than glucose. These observations support the conclusion that the progressive decline in glucose is not attributable to a loss in permeability of the microdialysis membrane.

The loss of detectable glucose in the dialysate comes as something of a surprise, considering that our histological studies indicate blood flow and NeuN-positive neurons at the probe track. It is important to mention that the absence of detectable glucose in the dialysate, while indicating a glucose aberration, does not necessarily imply an absence of glucose in the tissue. Dialysate levels of any substance, including glucose, reflect the balance between its delivery and removal from the interstitial space. Thus, a low dialysate glucose concentration indicates that glucose consumption (nonzero) in the tissue near the probe exceeds delivery via the vasculature, leaving insufficient glucose to be recovered by the microdialysis probe. Explaining whether the apparent imbalance is due to increased consumption, as is the case in glycolysis or decreased delivery, such as under ischemic conditions, is not possible with the data we have in hand: this will be the subject of a future report.

This study adds to a mounting body of evidence that Dex retrodialysis facilitates extended intracranial microdialysis in the rat brain over the course of at least 10, and possibly 12, days with a single probe insertion. The use of Dex in this manner represents a technical advance, given our previous difficulty with monitoring evoked dopamine release and pin-prick-induced CSDs 5 days after probe insertion without Dex.[14,79–81] We attribute these difficulties to the foreign-body response, rather than to probe failure per se. Dex retrodialysis offers the advantage of a single probe insertion as an alternative to extended microdialysis based on removal and replacement of multiple probes.[78] In the clinical setting, for example, removing and replacing multiple probes would not be medically practical.

In this work, Dex retrodialysis was combined with rapid measurements by the K+ ISE and the rsMD glucose analyzer.[56,71,80,103,104,106] This has facilitated real time monitoring of spontaneous CSDs at 10 and, in one case 12, days after CCI and probe insertion. Although

clinical 10-day microdialysis post injury has been reported before, those prior studies used 1-hr sampling times, which are much longer than CSDs.[126] Thus, herein we have documented a microdialysis protocol that uniquely combines extended monitoring with high temporal resolution. This study introduces extended Dex-enhanced microdialysis in the CCI rodent model of TBI as a new paradigm for investigating metabolic crisis in the injured brain.

5.0   CONCLUSIONS

This dissertation details several experiments involving implanted neuromonitoring devices. Electrochemical detection of DA with carbon fiber microelectrodes has the spatial and temporal resolution to prove that DA dynamics in the striatum are due to kinetics, not diffusion as previously thought. By applying mathematical modeling to electrically evoked DA responses, this work shows that an underlying basal autoinhibitory tone is the cause of fast and slow DA kinetic sites.

Slow sites have been essentially ignored in most research involving FSCV detection of DA. Slow sites have long been considered to be the result of poor electrode placement; researchers routinely move electrodes to optimize for fast sites, believing that slow sites are simply the result of electrodes placed too far from DA terminals.[86] However, the work presented in chapters 2 and 3 indicates that slow sites are the result of a basal autoinhibitory tone.

Additionally, unpublished work from Dr. Katy Nesbitt, Dr. Seth Walters, and Dr. Andrea Jaquins-Gerstl reveals that slow sites are associated with the matrix compartment of the DS, while the fast sites are associated with the striosomes. The striosome and matrix compartments have slightly different outputs, express several proteins differently, and are associated with varying symptoms of DA-related diseases, including Huntington's disease and Parkinson's disease.[29] The implication of these results is that essentially all research involving FSCV

detection of DA in the DS has been "optimized" to focus on just the striosomes, with the matrix compartment virtually ignored; this represents an enormous untapped area of research. Considering the vast amount of diseases and disorders DA is involved in, this is an enormous oversight.

Additionally, this work makes advances in the field of microdialysis monitoring of TBI patients. Dex-enhanced microdialysis has been shown in previous work to prevent gliosis from rendering the probe nonfunctional. However, the work presented here is the first time that Dex-enhanced microdialysis has been used to monitor in TBI model rats. Dex is still able to keep the probe functional even in the circumstance of a heightened immune response to the TBI itself. We were successfully able to detect CSDs and glucose and potassium levels for up to 12 days after CCI injury and probe implantation.

Recent advances involving the miniaturization of the rsMD system (now referred to as continuous online microdialysis (coMD) because it no longer requires dialysate to go through a sample loop) have made bedside Dex-enhanced microdialysis detection of brain glucose after TBI a possibility in human patients.[104,127] Brain glucose and blood glucose do not necessarily correlate, and low brain glucose levels have been shown to result in poorer outcomes for TBI and stroke patients.[108,126,128,129] The ability to monitor brain glucose levels in TBI patients long-term may one day be a standard of care that can alert physicians about the metabolic health of vulnerable patients.

BIBLIOGRAPHY

(1)   Haddad, S. H.; Arabi, Y. M. Critical Care Management of Severe Traumatic Brain Injury in Adults. *Scand. J. Trauma. Resusc. Emerg. Med.* **2012**, *20* (12), 1–15.

(2)   Ghajar, J. Traumatic Brain Injury. *Lancet* **2000**, *356* (9233), 923–929.

(3)   Carney, N.; Totten, A. M.; O'Reilly, C.; Ullman, J. S.; Hawryluk, G. W. J.; Bell, M. J.; Bratton, S. L.; Chesnut, R.; Harris, O. A.; Kissoon, N.; et al. Guidelines for the Management of Severe Traumatic Brain Injury, Fourth Edition. *Neurosurgery* **2017**, *80* (1), 6–15.

(4)   Vespa, P.; Bergsneider, M.; Hattori, N.; Wu, H. M.; Huang, S. C.; Martin, N. A.; Glenn, T. C.; McArthur, D. L.; Hovda, D. A. Metabolic Crisis without Brain Ischemia Is Common after Traumatic Brain Injury: A Combined Microdialysis and Positron Emission Tomography Study. *J. Cereb. Blood Flow Metab.* **2005**, *25* (6), 763–774.

(5)   Vespa, P. M.; Miller, C.; McArthur, D.; Eliseo, M.; Etchepare, M.; Hirt, D.; Glenn, T. C.; Martin, N.; Hovda, D. Nonconvulsive Electrographic Seizures after Traumatic Brain Injury Result in a Delayed, Prolonged Increase in Intracranial Pressure and Metabolic Crisis. *Crit. Care Med.* **2017**, *35* (12), 2830–2836.

(6)   Vespa, P.; Boonyaputthikul, R.; McArthur, D. L.; Miller, C.; Etchepare, M.; Bergsneider, M.; Glenn, T.; Martin, N.; Hovda, D. Intensive Insulin Therapy Reduces Microdialysis

Glucose Values without Altering Glucose Utilization or Improving the Lactate/Pyruvate Ratio after Traumatic Brain Injury. *Crit. Care Med.* **2006**, *34* (3), 850–856.

(7)   Rostami, E. Glucose and the Injured Brain-Monitored in the Neurointensive Care Unit. *Front. Neurol.* **2014**, *5* (91), 1–8.

(8)   Flesher, S. N.; Collinger, J. L.; Foldes, S. T.; Weiss, J. M.; Downey, J. E.; Tyler-Kabara, E. C.; Bensmaia, S. J.; Schwartz, A. B.; Boninger, M. L.; Gaunt, R. A. Intracortical Microstimulation of Human Somatosensory Cortex. *Sci. Transl. Med.* **2016**, *8* (361ra141), 1–10.

(9)   Collinger, J. L.; Wodlinger, B.; Downey, J. E.; Wang, W.; Tyler-Kabara, E. C.; Weber, D. J.; McMorland, A. J. C.; Velliste, M.; Boninger, M. L.; Schwartz, A. B. High-Performance Neuroprosthetic Control by an Individual with Tetraplegia. *Lancet* **2013**, *381* (9866), 557–564.

(10)   Wodlinger, B.; Downey, J. E.; Tyler-Kabara, E. C.; Schwartz, A. B.; Boninger, M. L.; Collinger, J. L. Ten-Dimensional Anthropomorphic Arm Control in a Human Brain-Machine Interface: Difficulties, Solutions, and Limitations. *J. Neural Eng.* **2015**, *12* (1).

(11)   Jaquins-Gerstl, A.; Michael, A. C. Comparison of the Brain Penetration Injury Associated with Microdialysis and Voltammetry. *J. Neurosci. Methods* **2009**, *183* (2), 127–135.

(12)   Taylor, I. M.; Ilitchev, A. I.; Michael, A. C. Restricted Diffusion of Dopamine in the Rat Dorsal Striatum. *ACS Chem. Neurosci.* **2013**, *4* (5), 870–878.

(13)   Jaquins-Gerstl, A.; Michael, A. C. A Review of the Effects of FSCV and Microdialysis Measurements on Dopamine Release in the Surrounding Tissue. *Analyst* **2015**, *140* (11), 3696–3708.

(14)   Nesbitt, K. M.; Jaquins-Gerstl, A.; Skoda, E. M.; Wipf, P.; Michael, A. C.

Pharmacological Mitigation of Tissue Damage during Brain Microdialysis. *Anal. Chem.* **2013**, *85* (17), 8173–8179.

(15) Kozai, T. D. Y.; Jaquins-Gerstl, A. S.; Vazquez, A. L.; Michael, A. C.; Cui, X. T. Brain Tissue Responses to Neural Implants Impact Signal Sensitivity and Intervention Strategies. *ACS Chem. Neurosci.* **2014**, *6*, 48–67.

(16) Walters, S. H.; Taylor, I. M.; Shu, Z.; Michael, A. C. A Novel Restricted Diffusion Model of Evoked Dopamine. *ACS Chem. Neurosci.* **2014**, *5* (9), 776–783.

(17) Walters, S. H.; Robbins, E. M.; Michael, A. C. Modeling the Kinetic Diversity of Dopamine in the Dorsal Striatum. *ACS Chem. Neurosci.* **2015**, *6* (8), 1468–1475.

(18) Walters, S. H.; Robbins, E. M.; Michael, A. C. The Kinetic Diversity of Striatal Dopamine: Evidence from a Novel Protocol for Voltammetry. *ACS Chem. Neurosci.* **2016**, *7* (5), 662–667.

(19) Horn, A. S.; Korf, J.; Westerink, B. H. C. *The Neurobiology of Dopamine*; Academic Press: London, 1979.

(20) Rosenberg, R. S.; Kosslyn, S. M. *Abnormal Psychology*; Worth Publishers: New York, 2010.

(21) Mannich, C.; Jacobsohn, W. Uber Oxyphenyl-Alkylamine Und Dioxyphenyl-Alkylamine. *Berichte der Dtsch. Chem. Gesellschaft* **1910**, *43* (1), 189–197.

(22) Carlsson, A.; Lindquist, M.; Magnusson, T. 3,4-Dihydroxyphenylalanine and 5-Hydroxytryptophan as Reserpine Antagonists. *Nature* **1957**, *180* (4596), 1200.

(23) Carlsson, A.; Lindquist, M.; Magnusson, T.; Waldeck, B. On the Presence of 3-Hydroxytyramine in Brain. *Science (80-.).* **1958**, *127* (3296), 471.

(24) Hornykiewicz, O. Dopamine (3-Hydroxytyramine) and Brain Function. *Pharmacol. Rev.*

1966, *18* (2), 925–964.

(25) Hornykiewicz, O. The Mechanisms of Action of L-Dopa in Parkinson's Disease. *Life Sci.* **1974**, *15* (7), 1249–1259.

(26) Kish, S. J.; Shannak, K.; Hornykiewicz, O. Uneven Pattern of Dopamine Loss in the Striatum of Patients with Idiopathic Parkinson's Disease. *N. Engl. J. Med.* **1988**, *318*, 876–880.

(27) Solanto, M. V. Dopamine Dysfunction in AD/HD: Integrating Clinical and Basic Neuroscience Research. *Behav. Brain Res.* **2002**, *130* (1–2), 65–71.

(28) Volkow, N. D.; Wang, G. J.; Telang, F.; Fowler, J. S.; Logan, J.; Childress, A. R.; Jayne, M.; Ma, Y.; Wong, C. Cocaine Cues and Dopamine in Dorsal Striatum: Mechanism of Craving in Cocaine Addiction. *J. Neurosci.* **2006**, *26* (24), 6583–6588.

(29) Crittenden, J. R.; Graybiel, A. M. Basal Ganglia Disorders Associated with Imbalances in the Striatal Striosome and Matrix Compartments. *Front. Neuroanat.* **2011**, *5* (59), 1–25.

(30) Rizzoli, S. O.; Betz, W. J. Synaptic Vesicle Pools. *Nat. Rev. Neurosci.* **2005**, *6* (1), 57–69.

(31) Rizzoli, S. O. Synaptic Vesicle Recycling. *Eur. Mol. Biol. Organ. J.* **2014**, *33* (8), 2014.

(32) Doucet, G.; Descarries, L.; Garcia, S. Quantification of the Dopamine Innervation in Adult Rat Neostriatum. *Neuroscience* **1986**, *19* (2), 427–435, 437–445.

(33) Garris, P. A.; Ciolkowski, E. L.; Pastore, P.; Wightman, R. M. Efflux of Dopamine from the Synaptic Cleft in the Nucleus Accumbens of the Rat Brain. *J. Neurosci.* **1994**, *4* (10), 6084–6093.

(34) Missale, C.; Nash, S. R. S.; Robinson, S. W.; Jaber, M.; Caron, M. G. Dopamine Receptors: From Structure to Function. *Physiol. Rev.* **1998**, *78* (1), 189–225.

(35) Probst, W. C.; Snyder, L. a; Schuster, D. I.; Brosius, J.; Sealfon, S. C. Sequence

Alignment of the G-Protein Coupled Receptor Superfamily. *DNA Cell Biol.* **1992**, *11* (1), 1–20.

(36) Becker, W. M.; Kleinsmith, L. J.; Hardin, J.; Bertoni, G. P. *The World of the Cell*; Pearson Education: San Francisco, 2009.

(37) Benoit-Marand, M.; Borrelli, E.; Gonon, F. Inhibition of Dopamine Release via Presynaptic D2 Receptors: Time Course and Functional Characteristics in Vivo. *J. Neurosci.* **2001**, *21* (23), 9134–9141.

(38) Moquin, K. F.; Michael, A. C. Tonic Autoinhibition Contributes to the Heterogeneity of Evoked Dopamine Release in the Rat Striatum. *J. Neurochem.* **2009**, *110* (5), 1491–1501.

(39) Laviron, E. Electrochemical Reacion with Protonations at Equilibrium Part VIII. *J. Electroanal. Chem.* **1983**, *143*, 15–36.

(40) Bard, A. J.; Faulkner, L. R. *Electrochemical Methods: Fundamentals and Applications*; John Wiley & Sons, Inc.: Hoboken, NJ, 2001.

(41) Ponchon, J. L.; Cespuglio, R.; Gonon, F.; Jouvet, M.; Pujol, J. F. Normal Pulse Polarography with Carbon Fiber Electrodes for in Vitro and in Vivo Determination of Catecholamines. *Anal. Chem.* **1979**, *51* (9), 1483–1486.

(42) Peters, J. L.; Miner, L. H.; Michael, A. C.; Sesack, S. R. Ultrastructure at Carbon Fiber Microelectrode Implantation Sites after Acute Voltammetric Measurements in the Striatum of Anesthetized Rats. *J. Neurosci. Methods* **2004**, *137* (1), 9–23.

(43) Taylor, I. M.; Jaquins-Gerstl, A.; Sesack, S. R.; Michael, A. C. Domain-Dependent Effects of DAT Inhibition in the Rat Dorsal Striatum. *J. Neurochem.* **2012**, *122* (2), 283–294.

(44) Borland, L. M.; Shi, G.; Yang, H.; Michael, A. C. Voltammetric Study of Extracellular

Dopamine near Microdialysis Probes Acutely Implanted in the Striatum of the Anesthetized Rat. *J. Neurosci. Methods* **2005**, *146* (2), 149–158.

(45) Jaquins-Gerstl, A.; Shu, Z.; Zhang, J.; Liu, Y.; Weber, S. G.; Michael, A. C. Effect of Dexamethasone on Gliosis, Ischemia, and Dopamine Extraction during Microdialysis Sampling in Brain Tissue. *Anal. Chem.* **2011**, *83* (20), 7662–7667.

(46) Andrieux, C. P.; Garreau, D.; Hapiot, P.; Pinson, J.; Saveant, J. M. Fast Sweep Cyclic Voltammetry at Ultra-Microelectrodes: Evaluation of the Method for Fast Electron-Transfer Kinetic Measurements. *J. Electroanal. Chem.* **1988**, *243*, 321–335.

(47) Amatore, C.; Arbault, S.; Guille, M.; Lemaître, F. Electrochemical Monitoring of Single Cell Secretion: Vesicular Exocytosis and Oxidative Stress. *Chem. Rev.* **2008**, *108* (7), 2585–2621.

(48) Bath, B. D.; Michael, D. J.; Trafton, B. J.; Joseph, J. D.; Runnels, P. L.; Wightman, R. M. Subsecond Adsorption and Desorption of Dopamine at Carbon-Fiber Microelectrodes. *Anal. Chem.* **2000**, *72* (24), 5994–6002.

(49) Bath, B. D.; Martin, H. B.; Wightman, R. M.; Anderson, M. R. Dopamine Adsorption at Surface Modified Carbon-Fiber Electrodes. *Langmuir* **2001**, *17* (22), 7032–7039.

(50) Bruns Jr, J.; Hauser, W. A. The Epidemiology of Traumatic Brain Injury: A Review. *Epilepsia* **2003**, *44* (Suppl. 10), 2–10.

(51) Pietrobon, D.; Moskowitz, M. A. Chaos and Commotion in the Wake of Cortical Spreading Depression and Spreading Depolarizations. *Nat. Rev. Neurosci.* **2014**, *15* (6), 379–393.

(52) Dreier, J. P.; Fabricius, M.; Ayata, C.; Sakowitz, O. W.; Shuttleworth, C. W.; Dohmen, C.; Graf, R.; Vajkoczy, P.; Helbok, R.; Suzuki, M.; et al. Recording, Analysis, and

Interpretation of Spreading Depolarizations in Neurointensive Care: Review and Recommendations of the COSBID Research Group. *J. Cereb. Blood Flow Metab.* **2017**, *37* (5), 1595–1625.

(53)   Feuerstein, D.; Manning, A.; Hashemi, P.; Bhatia, R.; Fabricius, M.; Tolias, C.; Pahl, C.; Ervine, M.; Strong, A. J.; Boutelle, M. G. Dynamic Metabolic Response to Multiple Spreading Depolarizations in Patients with Acute Brain Injury: An Online Microdialysis Study. *J. Cereb. Blood Flow Metab.* **2010**, *30* (7), 1343–1355.

(54)   Dreier, J. P.; Woitzik, J.; Fabricius, M.; Bhatia, R.; Major, S.; Drenckhahn, C.; Lehmann, T. N.; Sarrafzadeh, A.; Willumsen, L.; Hartings, J. A.; et al. Delayed Ischaemic Neurological Deficits after Subarachnoid Haemorrhage Are Associated with Clusters of Spreading Depolarizations. *Brain* **2006**, *129* (12), 3224–3237.

(55)   Fabricius, M.; Fuhr, S.; Willumsen, L.; Dreier, J. P.; Bhatia, R.; Boutelle, M. G.; Hartings, J. A.; Bullock, R.; Strong, A. J.; Lauritzen, M. Association of Seizures with Cortical Spreading Depression and Peri-Infarct Depolarisations in the Acutely Injured Human Brain. *Clin. Neurophysiol.* **2008**, *119*, 1973–1984.

(56)   Papadimitriou, K. I.; Wang, C.; Rogers, M. L.; Gowers, S. A. N.; Leong, C. L.; Boutelle, M. G. High-Performance Bioinstrumentation for Real-Time Neuroelectrochemical Traumatic Brain Injury Monitoring. *Front. Hum. Neurosci.* **2016**, *10* (212), 1–15.

(57)   Hartings, J. A.; Bullock, M. R.; Okonkwo, D. O.; Murray, L. S.; Murray, G. D.; Fabricius, M.; Maas, A. I. R.; Woitzik, J.; Sakowitz, O.; Mathern, B.; et al. Spreading Depolarisations and Outcome after Traumatic Brain Injury: A Prospective Observational Study. *Lancet Neurol.* **2011**, *10* (12), 1058–1064.

(58)   Leão, A. A. Spreading Depression of Activity in the Cerebral Cortex. *J. Neurophysiol.*

1944, *7*, 359–390.

(59)   Jalloh, I.; Carpenter, K. L. H.; Helmy, A.; Carpenter, T. A.; Menon, D. K.; Hutchinson, P. J. Glucose Metabolism Following Human Traumatic Brain Injury: Methods of Assessment and Pathophysiological Findings. *Metab. Brain Dis.* **2015**, *30* (3), 615–632.

(60)   Carpenter, K. L. H.; Jalloh, I.; Hutchinson, P. J. Glycolysis and the Significance of Lactate in Traumatic Brain Injury. *Front. Neurosci.* **2015**, *9* (APR), 1–15.

(61)   Watson, C. J.; Venton, B. J.; Kennedy, R. T. In Vivo Measurements of Neurotransmitters by Microdialysis Sampling. *Anal. Chem.* **2006**, *78* (5), 1391–1399.

(62)   Wightman, R. M. Monitoring Molecules: Insights and Progress. *ACS Chem. Neurosci.* **2015**, *6*, 5–7.

(63)   Rogers, M. L.; Boutelle, M. G. Real-Time Clinical Monitoring of Biomolecules. *Annu. Rev. Anal. Chem.* **2013**, *6* (1), 427–453.

(64)   Delgado, J. M.; DeFeudis, F. V; Roth, R. H.; Ryugo, D. K.; Mitruka, B. M. Dialytrode for Long Term Intracerebral Perfusion in Awake Monkeys. *Arch. Int. Pharmacodyn. Ther.* **1972**, *198* (1), 9–21.

(65)   Ungerstedt, U.; Pycock, C. Functional Correlates of Dopamine Neurotransmission. *Bull. Schweiz. Akad. Med. Wiss.* **1974**, *30*, 44–55.

(66)   Westerink, B. H. C.; Damsma, G.; Rollema, H.; De Vries, J. B.; Horn, A. S. Scope and Limitations of in Vivo Brain Dialysis: A Comparison of Its Application to Various Neurotransmitter Systems. *Life Sci.* **1987**, *41* (15), 1763–1776.

(67)   Gu, H.; Varner, E. L.; Groskreutz, S. R.; Michael, A. C.; Weber, S. G. In Vivo Monitoring of Dopamine by Microdialysis with 1 Min Temporal Resolution Using Online Capillary Liquid Chromatography with Electrochemical Detection. *Anal. Chem.* **2015**, *87*, 6088–

6094.

(68) Ngo, K. T.; Varner, E. L.; Michael, A. C.; Weber, S. G. Monitoring Dopamine Responses to Potassium Ion and Nomifensine by in Vivo Microdialysis with Online Liquid Chromatography at One-Minute Resolution. *ACS Chem. Neurosci.* **2017**, *8*, 329–338.

(69) Haskins, W. E.; Wang, Z.; Watson, C. J.; Rostand, R. R.; Witowski, S. R.; Powell, D. H.; Kennedy, R. T. Capillary LC-MS 2 at the Attomole Level for Monitoring and Discovering Endogenous Peptides in Microdialysis Samples Collected in Vivo. *Anal. Chem.* **2001**, *73* (21), 5005–5014.

(70) Song, P.; Hershey, N. D.; Mabrouk, O. S.; Slaney, T. R.; Kennedy, R. T. Mass Spectrometry "Sensor" for in Vivo Acetylcholine Monitoring. *Anal. Chem.* **2012**, *84* (11), 4659–4664.

(71) Hopwood, S. E.; Parkin, M. C.; Bezzina, E. L.; Boutelle, M. G.; Strong, A. J. Transient Changes in Cortical Glucose and Lactate Levels Associated with Peri-Infarct Depolarisations, Studied with Rapid-Sampling Microdialysis. *J. Cereb. Blood Flow Metab.* **2005**, *25* (3), 391–401.

(72) Hamaoui, K.; Gowers, S.; Damji, S.; Rogers, M.; Leong, C. L.; Hanna, G.; Darzi, A.; Boutelle, M.; Papalois, V. Rapid Sampling Microdialysis as a Novel Tool for Parenchyma Assessment during Static Cold Storage and Hypothermic Machine Perfusion in a Translational Ex Vivo Porcine Kidney Model. *J. Surg. Res.* **2015**, *200* (1), 332–345.

(73) Justice Jr., J. B. Quantitative Microdialysis of Neurotransmitters. *J. Neurosci. Methods* **1993**, *48* (3), 263–276.

(74) Yang, H.; Peters, J. L.; Allen, C.; Chern, S. S.; Coalson, R. D.; Michael, A. C. A Theoretical Description of Microdialysis with Mass Transport Coupled to Chemical

Events. *Anal. Chem.* **2000**, *72* (9), 2042–2049.

(75)   Santiago, M.; Westerink, B. H. C. Characterization of the in Vivo Release of Dopamine as Recorded by Different Types of Intracerebral Microdialysis Probes. *Naunyn. Schmiedebergs. Arch. Pharmacol.* **1990**, *342* (4), 407–414.

(76)   DeBoer, P.; Abercrombie, E. D. Physiological Release of Striatal Acetylcholine in Vivo: Modulation by D1 and D2 Dopamine Receptor Subtypes. *J. Pharmacol. Exp. Ther.* **1996**, *277* (2), 775–783.

(77)   Markwardt, N. T.; Stokol, J.; Rennaker II, R. L. Sub-Meninges Implantation Reduces Immune Response to Neural Implants. *J. Neurosci. Methods* **2013**, *214* (2), 119–125.

(78)   Di Chiara, G.; Tanda, G.; Carboni, E. Estimation of In-Vivo Neurotransmitter Release by Brain Microdialysis: The Issue of Validity. *Behav. Pharmacol.* **1996**, *7* (7), 640–657.

(79)   Nesbitt, K. M.; Varner, E. L.; Jaquins-Gerstl, A.; Michael, A. C. Microdialysis in the Rat Striatum: Effects of 24 h Dexamethasone Retrodialysis on Evoked Dopamine Release and Penetration Injury. *ACS Chem. Neurosci.* **2015**, *6* (1), 163–173.

(80)   Varner, E. L.; Leong, C. L.; Jaquins-Gerstl, A.; Nesbitt, K. M.; Boutelle, M. G.; Michael, A. C. Enhancing Continuous Online Microdialysis Using Dexamethasone: Measurement of Dynamic Neurometabolic Changes during Spreading Depolarization. *ACS Chem. Neurosci.* **2017**.

(81)   Varner, E. L.; Jaquins-Gerstl, A.; Michael, A. C. Enhanced Intracranial Microdialysis by Reduction of Traumatic Penetration Injury at the Probe Track. *ACS Chem. Neurosci.* **2016**.

(82)   Engstrom, R. C.; Wightman, R. M.; Kristensen, E. W. Diffusional Distortion in the Monitoring of Dynamic Events. *Anal. Chem.* **1988**, *60* (7), 652–656.

(83)   Schroeder, T. J.; Jankowski, J. A.; Kawagoe, K. T.; Wightman, R. M.; Lefrou, C.; Amatore, C. Analysis of Diffusional Broadening of Vesicular Packets of Catecholamines Released from Biological Cells during Exocytosis. *Anal. Chem.* **1992**, *64* (24), 3077–3083.

(84)   Moquin, K. F.; Michael, A. C. An Inverse Correlation between the Apparent Rate of Dopamine Clearance and Tonic Autoinhibition in Subdomains of the Rat Striatum: A Possible Role of Transporter-Mediated Dopamine Efflux. *J. Neurochem.* **2011**, *117* (1), 133–142.

(85)   Wightman, R. M.; Amatore, C.; Engstrom, R. C.; Halea, P. D.; Kristensena, E. W.; Kuhra, W. G.; Maya, L. J.; Hale, P. D.; Kristensen, E. W.; Kuhr, W. G.; et al. Real-Time Characterization of Dopamine Overflow and Uptake in the Rat Striatum. *Neuroscience* **1988**, *25* (2), 513–523.

(86)   Venton, J.; Zhang, H.; Garris, P. A.; Phillips, P. E. M.; Sulzer, D.; Wightman, R. M. Real-Time Decoding of Dopamine Concentration Changes in the Caudate-Putamen during Tonic and Phasic Firing. *J. Neurochem.* **2003**, *87* (5), 1284–1295.

(87)   Nicholson, C.; Rice, M. E. *Volume Transmission in the Brain*; Raven Press: New York, 1991.

(88)   Venton, B. J.; Seipel, A. T.; Phillips, P. E. M.; Wetsel, W. C.; Gitler, D.; Greengard, P.; Augustine, G.; Wightman, R. M. Cocaine Increases Dopamine Release by Mobilization of a Synapsin-Dependent Reserve Pool. *J. Neurosci.* **2006**, *26* (12), 3206–3209.

(89)   Jaffe, E. H.; Marty, A.; Schulte, A.; Chow, R. H. Extrasynaptic Vesicular Transmitter Release from the Somata of Substantia Nigra Neurons in Rat Midbrain Slices. *J. Neurosci.* **2018**, *18* (10), 3548–3553.

(90) Puthongkham, P.; Yang, C.; Venton, B. J. Carbon Nanohorn-Modified Carbon Fiber Microelectrodes for Dopamine Detection. *Electroanalysis* **2018**, *30* (6), 1073–1081.

(91) Gómez-A, A.; Shnitko, T. A.; Barefoot, H. M.; Brightbill, E. L.; Sombers, L. A.; Nicola, S. M.; Robinson, D. L. Local μ-Opioid Receptor Antagonism Blunts Evoked Phasic Dopamine Release in the Nucleus Accumbens of Rats. *ACS Chem. Neurosci.* **2019**, *10* (4), 1935–1940.

(92) Spanos, M.; Xie, X.; Gras-Najjar, J.; White, S. C.; Sombers, L. A. NMDA Receptor-Dependent Cholinergic Modulation of Mesolimbic Dopamine Cell Bodies: Neurochemical and Behavioral Studies. *ACS Chem. Neurosci.* **2019**, *10* (3), 1497–1505.

(93) Pyakurel, P.; Shin, M.; Venton, B. J. Nicotinic Acetylcholine Receptor (NAChR) Mediated Dopamine Release in Larval Drosophila Melanogaster. *Neurochem. Int.* **2018**, *114*, 33–41.

(94) Wu, Q.; Reith, M. E. A.; Wightman, R. M.; Kawagoe, K. T.; Garris, P. A. Determination of Release and Uptake Parameters from Electrically Evoked Dopamine Dynamics Measured by Real-Time Voltammetry. *J. Neurosci. Methods* **2001**, *112*, 119–133.

(95) Garris, P. A.; Rebec, G. V. Modeling Fast Dopamine Neurotransmission in the Nucleus Accumbens during Behavior. *Behav. Brain Res.* **2002**, *137* (1–2), 47–63.

(96) Taylor, I. M.; Nesbitt, K. M.; Walters, S. H.; Varner, E. L.; Shu, Z.; Bartlow, K. M.; Jaquins-Gerstl, A. S.; Michael, A. C. Kinetic Diversity of Dopamine Transmission in the Dorsal Striatum. *J. Neurochem.* **2015**, *133* (4), 522–531.

(97) Shu, Z.; Taylor, I. M.; Michael, A. C. The Dopamine Patchwork of the Rat Nucleus Accumbens Core. *Eur. J. Neurosci.* **2013**, *38* (8), 3221–3229.

(98) Shu, Z.; Taylor, I. M.; Walters, S. H.; Michael, A. C. Region- and Domain-Dependent

Action of Nomifensine. *Eur. J. Neurosci.* **2014**, No. February, 1–9.

(99) Wang, Y.; Moquin, K. F.; Michael, A. C. Evidence for Coupling between Steady-State and Dynamic Extracellular Dopamine Concentrations in the Rat Striatum. *J. Neurochem.* **2010**, *114* (1), 150–159.

(100) Dickinson, S. D.; Sabeti, J.; Larson, G. A.; Giardina, K.; Rubinstein, M.; Kelly, M. A.; Grandy, D. K.; Low, M. J.; Gerhardt, G. A.; Zahniser, N. R. Dopamine D2 Receptor-Deficient Mice Exhibit Decreased Dopamine Transporter Function but No Changes in Dopamine Release in Dorsal Striatum. *J. Neurochem.* **1999**, *72* (1), 148–156.

(101) Cass, W. A.; Gerhardt, G. A. Direct in Vivo Evidence That D2 Dopamine Receptors Can Modulate Dopamine Uptake. *Neurosci. Lett.* **1994**, *176* (2), 259–263.

(102) Dohmen, C.; Sakowitz, O. W.; Fabricius, M.; Bosche, B.; Reithmeier, T.; Ernestus, R.; Brinker, G.; Dreier, J. P.; Woitzik, J.; Strong, A. J.; et al. Spreading Depolarizations Occur in Human Ischemic Stroke with High Incidence. *Ann. Neurol.* **2008**, *63* (6), 720–728.

(103) Parkin, M. C.; Hopwood, S. E.; Jones, D. A.; Hashemi, P.; Landolt, H.; Fabricius, M.; Lauritzen, M.; Boutelle, M. G.; Strong, A. J. Dynamic Changes in Brain Glucose and Lactate in Pericontusional Areas of the Human Cerebral Cortex, Monitored with Rapid Sampling on-Line Microdialysis: Relationship with Depolarisation-like Events. *J. Cereb. Blood Flow Metab.* **2005**, *25* (3), 402–413.

(104) Rogers, M. L.; Feuerstein, D.; Leong, C. L.; Takagaki, M.; Niu, X.; Graf, R.; Boutelle, M. G. Continuous Online Microdialysis Using Microfluidic Sensors: Dynamic Neurometabolic Changes during Spreading Depolarization. *ACS Chem. Neurosci.* **2013**, *4* (5), 799–807.

(105) Hartings, J. A.; Watanabe, T.; Bullock, M. R.; Okonkwo, D. O.; Fabricius, M.; Woitzik,

J.; Dreier, J. P.; Puccio, A.; Shutter, L. A.; Pahl, C.; et al. Spreading Depolarizations Have Prolonged Direct Current Shifts and Are Associated with Poor Outcome in Brain Trauma. *Brain* **2011**, *134* (5), 1529–1540.

(106) Bhatia, R.; Hashemi, P.; Razzaq, A.; Parkin, M. C.; Hopwood, S. E.; Boutelle, M. G.; Strong, A. J. Application of Rapid-Sampling, Online Microdialysis to the Monitoring of Brain Metabolism during Aneurysm Surgery. *Neurosurgery* **2006**, *58* (Operative Neuroscurgery 2), 313–321.

(107) De Lima Oliveira, M.; Kairalla, A. C.; Fonoff, E. T.; Martinez, R. C. R.; Teixeira, M. J.; Bor-Seng-Shu, E. Cerebral Microdialysis in Traumatic Brain Injury and Subarachnoid Hemorrhage: State of the Art. *Neurocrit. Care* **2014**, *21* (1), 152–162.

(108) Griesdale, D. E. G.; Tremblay, M. H.; McEwen, J.; Chittock, D. R. Glucose Control and Mortality in Patients with Severe Traumatic Brain Injury. *Neurocrit. Care* **2009**, *11* (3), 311–316.

(109) Guiou, M.; Sheth, S.; Nemoto, M.; Walker, M.; Pouratian, N.; Ba, A.; Toga, A. W. Cortical Spreading Depression Produces Long-Term Disruption of Activity-Related Changes in Cerebral Blood Volume and Neurovascular Coupling. *J. Biomed. Opt.* **2005**, *10* (1), 011004.

(110) Hartings, J. A.; Rolli, M. L.; Lu, X.-C. M.; Tortella, F. C. Delayed Secondary Phase of Peri-Infacrt Depolarizations after Focal Cerebral Ischemia: Relation to Infarct Growth and Neuroprotection. *J. Neurosci.* **2003**, *23* (37), 11602–11610.

(111) Seule, M.; Keller, E.; Unterberg, A.; Sakowitz, O. The Hemodynamic Response of Spreading Depolarization Observed by Near Infrared Spectroscopy After Aneurysmal Subarachnoid Hemorrhage. *Neurocrit. Care* **2015**, *23* (1), 108–112.

(112) Kozai, T. D. Y.; Jaquins-Gerstl, A. S.; Vazquez, A. L.; Michael, A. C.; Cui, X. T. Dexamethasone Retrodialysis Attenuates Microglial Response to Implanted Probes in Vivo. *Biomaterials* **2016**, *87*, 157–169.

(113) Shain, W.; Spataro, L.; Dilgen, J.; Haverstick, K.; Retterer, S.; Isaacson, M.; Saltzman, M.; Turner, J. N. Controlling Cellular Reactive Responses around Neural Prosthetic Devices Using Peripheral and Local Intervention Strategies. *IEEE Trans. Neural Syst. Rehabil. Eng.* **2003**, *11* (2), 186–188.

(114) Wagner, A. K.; Sokoloski, J. E.; Ren, D.; Chen, X.; Khan, A. S.; Zafonte, R. D.; Michael, A. C.; Dixon, C. E. Controlled Cortical Impact Injury Affects Dopaminergic Transmission in the Rat Striatum. *J. Neurochem.* **2005**, *95* (2), 457–465.

(115) Xiong, Y.; Mahmood, A.; Chopp, M. Animal Models of Traumatic Brain Injury. *Nat. Rev. Neurosci.* **2013**, *14*, 128–142.

(116) Dixon, C. E.; Clifton, G. L.; Lighthall, J. W.; Yaghmai, A. A.; Hayes, R. L. A Controlled Cortical Impact Model of Traumatic Brain Injury in the Rat. *J. Neurosci. Methods* **1991**, *39* (3), 253–262.

(117) Rogers, M. L.; Brennan, P. A.; Leong, C. L.; Gowers, S. A. N.; Aldridge, T.; Mellor, T. K.; Boutelle, M. G. Online Rapid Sampling Microdialysis (RsMD) Using Enzyme-Based Electroanalysis for Dynamic Detection of Ischaemia during Free Flap Reconstructive Surgery. *Anal. Bioanal. Chem.* **2013**, *405* (11), 3881–3888.

(118) Rogers, M. L.; Leong, C. L.; Gowers, S. A. N.; Samper, I. C.; Jewell, S. L.; Khan, A.; McCarthy, L.; Pahl, C.; Tolias, C. M.; Walsh, D. C.; et al. Simultaneous Monitoring of Potassium, Glucose and Lactate during Spreading Depolarization in the Injured Human Brain – Proof of Principle of a Novel Real-Time Neurochemical Analysis System,

Continuous Online Microdialysis. *J. Cereb. Blood Flow Metab.* **2017**, *37* (5), 1883–1895.

(119) Bosche, B.; Graf, R.; Ernestus, R. I.; Dohmen, C.; Reithmeier, T.; Brinker, G.; Strong, A. J.; Dreier, J. P.; Woitzik, J. Recurrent Spreading Depolarizations after Subarachnoid Hemorrhage Decreases Oxygen Availability in Human Cerebral Cortex. *Ann. Neurol.* **2010**, *67* (5), 607–617.

(120) Strong, A. J.; Fabricius, M.; Boutelle, M. G.; Hibbins, S. J.; Hopwood, S. E.; Jones, R.; Parkin, M. C.; Lauritzen, M. Spreading and Synchronous Depressions of Cortical Activity in Acutely Injured Human Brain. *Stroke* **2002**, *33* (12), 2738–2743.

(121) Somjen, G. G. Mechanisms of Spreading Depression and Hypoxic Spreading Depression-Like Depolarization. *Physiol. Rev.* **2001**, *81* (3), 1065–1096.

(122) Lauritzen, M.; Dreier, J. P.; Fabricius, M.; Hartings, J. A.; Graf, R.; Strong, A. J. Clinical Relevance of Cortical Spreading Depression in Neurological Disorders: Migraine, Malignant Stroke, Subarachnoid and Intracranial Hemorrhage, and Traumatic Brain Injury. *J. Cereb. Blood Flow Metab.* **2011**, *31* (1), 17–35.

(123) Ayata, C.; Lauritzen, M. Spreading Depression, Spreading Depolarizations, and the Cerebral Vasculature. *Physiol. Rev.* **2015**, *95* (3), 953–993.

(124) Hall, C. N.; Reynell, C.; Gesslein, B.; Hamilton, N. B.; Mishra, A.; Sutherland, B. A.; O'Farrell, F. M.; Buchan, A. M.; Lauritzen, M.; Attwell, D. Capillary Pericytes Regulate Cerebral Blood Flow in Health and Disease. *Nature* **2014**, *508* (7494), 55–60.

(125) Balança, B.; Meiller, A.; Bezin, L.; Dreier, J. P.; Marinesco, S.; Lieutaud, T. Altered Hypermetabolic Response to Cortical Spreading Depolarizations after Traumatic Brain Injury in Rats. *J. Cereb. Blood Flow Metab.* **2017**, *37* (5), 1670–1686.

(126) Vespa, P. M.; McArthur, D.; O'Phelan, K.; Glenn, T.; Etchepare, M.; Kelly, D.;

Bergsneider, M.; Martin, N. A.; Hovda, D. A. Persistently Low Extracellular Glucose Correlates with Poor Outcome 6 Months after Human Traumatic Brain Injury despite a Lack of Increased Lactate: A Microdialysis Study. *J. Cereb. Blood Flow Metab.* **2003**, *23* (7), 865–877.

(127) Gowers, S. A. N.; Curto, V. F.; Seneci, C. A.; Wang, C.; Anastasova, S.; Vadgama, P.; Yang, G. Z.; Boutelle, M. G. 3D Printed Microfluidic Device with Integrated Biosensors for Online Analysis of Subcutaneous Human Microdialysate. *Anal. Chem.* **2015**, *87* (15), 7763–7770.

(128) Shi, J.; Dong, B.; Mao, Y.; Guan, W.; Cao, J.; Zhu, R.; Wang, S. Review: Traumatic Brain Injury and Hyperglycemia, a Potentially Modifiable Risk Factor. *Oncotarget* **2015**, *7* (43), 71052–71061.

(129) Vespa, P.; McArthur, D. L.; Stein, N.; Huang, S. C.; Shao, W.; Filippou, M.; Etchepare, M.; Glenn, T.; Hovda, D. A. Tight Glycemic Control Increases Metabolic Distress in Traumatic Brain Injury: A Randomized Controlled within-Subjects Trial. *Crit. Care Med.* **2012**, *40* (6), 1923–1929.